Boron isotope record of peak metamorphic ultrahigh-pressure and retrograde fluid-rock interaction in white mica (Lago di Cignana, Western Alps)

Ralf Halama[1*], Matthias Konrad-Schmolke[2], Jan C.M. De Hoog[3]

[1] School of Geography, Geology and the Environment, Keele University, Keele, ST5 5BG, United Kingdom

[2] Department of Earth Sciences, University of Gothenburg, Guldhedsgatan 5a, 41320 Sweden

[3] School of GeoSciences, Grant Institute, James Hutton Road, Edinburgh, EH9 3FE, United Kingdom

[*] Corresponding author; e-mail: r.halama@keele.ac.uk; phone: 0044-1782-734960

ORCID:

Ralf Halama: 0000-0002-9770-6784

Matthias Konrad-Schmolke: 0000-0002-5607-3108

Jan C.M. De Hoog: 0000-0002-5930-3597

Abstract

This study presents boron (B) concentration and isotope data for white mica from (ultra)high-pressure (UHP), subduction-related metamorphic rocks from Lago di Cignana (Western Alps, Italy). These rocks are of specific geological interest because they comprise the most deeply subducted rocks of oceanic origin worldwide. Boron geochemistry can track fluid-rock interaction during their metamorphic evolution and provide important insights into mass transfer processes in subduction zones.

The highest B contents (up to 345 µg/g B) occur in peak metamorphic phengite from a garnet-phengite quartzite. The B isotopic composition is variable ($\delta^{11}B$ = -10.3 to -3.6 ‰) and correlates positively with B concentrations. Based on similar textures and major element mica composition, neither textural differences, prograde growth zoning, diffusion nor a retrograde overprint can explain this correlation. Modelling shows that B devolatilization during metamorphism can explain the general trend, but fails to account for the wide compositional and isotopic variability in a single, well-equilibrated sample. We therefore argue that this trend represents fluid-rock interaction during peak metamorphic conditions. This interpretation is supported by fluid-rock interaction modelling of boron leaching and boron addition that can successfully reproduce the observed spread in $\delta^{11}B$ and [B]. Taking into account the local availability of serpentinites as potential source rocks of the fluids, the temperatures reached during peak metamorphism that allow for serpentine dehydration, and the high positive $\delta^{11}B$ values ($\delta^{11}B$ = 20±5) modelled for the fluids, an influx of serpentinite-derived fluid appears likely.

Paragonite in lawsonite pseudomorphs in an eclogite and phengite from a retrogressed metabasite have B contents between 12 and 68 µg/g and $\delta^{11}B$ values that cluster around 0 ‰ ($\delta^{11}B$ = -5.0 to +3.5). White mica in both samples is related to distinct stages of retrograde metamorphism during exhumation of the rocks. The variable B geochemistry can be successfully modelled as fluid-rock

interaction with low to moderate (<3) fluid/rock ratios, where mica equilibrates with a fluid into which B preferentially partitions, causing leaching of B from the rock.

The metamorphic rocks from Lago di Cignana show variable retention of B in white mica during subduction-related metamorphism and exhumation. The variability in the B geochemical signature in white mica is significant and enhances our understanding of metamorphic processes and their role in element transfer in subduction zones.

Keywords:

Boron isotopes, white mica, subduction, metamorphism, fluid-rock interaction, devolatilization

Introduction

Boron (B) and the B stable isotope system are useful tracers of fluid-mediated mass transfer in subduction zones. Boron elemental and isotopic data can be used to track water cycling and the origin of fluid sources in subduction zone magmatism (Marschall et al. 2007; Konrad-Schmolke and Halama 2014; De Hoog and Savov 2018) as well as fluid-rock interaction processes and metasomatism in the metamorphic evolution of subduction-related metamorphic rocks (Bebout and Nakamura 2003; Marschall et al. 2006b, 2009; Halama et al. 2014). Across-arc profiles in arc lavas show a systematic and coupled decrease in B concentrations and B isotopic compositions (Ishikawa and Nakamura 1994; Ishikawa et al. 2001). These trends have been attributed to a decreasing addition of slab-derived fluids with increasing slab depth (Bebout et al. 1999; Peacock and Hervig 1999; Rosner et al. 2003) based on the preferential partitioning of B into the fluid (Brenan et al. 1998) and the large isotopic fractionation of the two stable B isotopes (^{11}B and ^{10}B) with a relative preference of the heavy isotope ^{11}B for the fluid (Wunder et al. 2005; Sanchez-Valle et al. 2005). Consequently, slab dehydration is expected to lead to successively decreasing $\delta^{11}B$ values in the dehydrating rocks of the subducting slab (Moran et al. 1992; Marschall et al. 2007; Konrad-Schmolke and Halama 2014). Whole-rock analyses of high-pressure metamorphic rocks have also shown that B correlates positively with H_2O contents and traces progressive dehydration (Marschall et al. 2009; Scambelluri et al. 2004), which can be used to model across-arc variations in volcanic rocks that show systematic trends in B geochemistry (Konrad-Schmolke et al. 2016).

Several studies have focused on tourmaline as the major B-hosting phase to track the B isotopic evolution of fluids in subduction zone settings (Bebout and Nakamura 2003; Marschall et al., 2006b; Ota et al., 2008). However, as tourmaline is absent in many lithologies, white mica (phengite, muscovite and/or paragonite), can act as a major mineral host for B, which substitutes for tetrahedrally coordinated aluminium (Wunder et al. 2005). Since white mica is stable over a wide range of temperatures and pressures in subduction-related metamorphic rocks and common in both meta-

igneous and metasedimentary rocks, it is a suitable alternative to investigate B systematics (e.g. Peacock and Hervig 1999; Pabst et al. 2012; Trumbull and Slack 2018). Subsequent work showed that the complex interplay of dehydration and rehydration during exhumation, deformation and metasomatic events could be traced in zoned white mica from subduction-related rocks utilizing B as an indicative element (Konrad-Schmolke et al. 2011; Angiboust et al. 2014; Halama et al. 2014; Sievers et al. 2017).

In this study, we investigate the B concentrations and B isotope composition of white mica in (ultra)high-pressure (UHP) metamorphic rocks from Lago di Cignana (Western Alps, Italy). We investigate three different lithologies - a garnet-phengite quartzite, an eclogite and a retrogressed metabasite - that have experienced a similar P/T evolution in a subduction zone setting. Fluid-rock interaction models successfully match the data for both peak metamorphic and retrogressed samples, demonstrating that boron measurements in white mica are a sensitive probe into fluid-rock interaction processes and emphasizes the role of intergranular fluids for element mobility and transfer even at ultrahigh-pressure metamorphic conditions.

Geological setting

A belt of subduction-related (U)HP metamorphic rocks in the Western Alps stretches from the Mediterranean Sea to Switzerland (Fig. 1). These rocks are part of the Penninic Domain in the Alps, which represent remnants of the Tethys Ocean (or Piemonte-Liguria Ocean) between the European continent to the NW and the Apulia plate to the SE (Dal Piaz 1974). The Penninic Domain comprises igneous oceanic crust of the Tethys Ocean (Piemonte-Liguria Ocean) and the sedimentary cover that was deposited along its European continental margin (Beltrando et al. 2010). The subduction-related (U)HP rocks underwent Alpine metamorphism and constitute the Piemonte Zone, which can be subdivided into an eclogite facies Zermatt-Saas Zone and a greenschist- to blueschist-facies Combin

85 Zone (Fig. 1). In the Zermatt-Saas zone, bodies of Fe-Ti gabbros converted to eclogites and Mg-Al
86 gabbros occur with serpentinized mantle peridotites. The serpentinites are locally overlain by
87 metasediments (calcschists and impure quartzites) and/or pillow lavas representing meta-ophiolitic
88 lithologies (Beltrando et al. 2010). Peak metamorphic pressures were reached at 48-44 Ma before
89 juxtaposition of the Zermatt-Saas with the Combin Zone at around 38 Ma (Rubatto et al. 1998; Reddy
90 et al. 1999; Lapen et al. 2003; Beltrando et al. 2009).
91 At the Lago di Cignana in the Valtournenche, NW Italy (Fig. 1), tectonic slices of meta-ophiolites of
92 the Zermatt-Saas Zone enclose a coesite- and diamond-bearing UHP metamorphic unit, the Lago di
93 Cignana Unit (LCU) (Pleuger et al. 2007; Groppo et al. 2009; Frezzotti et al. 2011). The lithologies
94 of the LCU represent former oceanic crust and comprise metabasites and metasedimentary rocks
95 (Compagnoni and Rolfo 2003). Metabasites of the LCU are geochemically similar to those of the
96 Zermatt-Saas Zone, showing a typical mid-ocean ridge basalt (MORB) signature with an oceanic
97 tholeiitic parentage. The metasedimentary rocks comprise impure marbles and quartzites, calcschists
98 and Mn-rich garnetites with Fe-Mn nodules (Bearth 1967; Dal Piaz et al. 1979). Garnets from these
99 metasedimentary rocks contain microdiamond inclusions (Frezzotti et al. 2011, 2014).
100
101 FIGURE 1 ABOUT HERE
102
103 The prograde metamorphic evolution of the LCU was reconstructed for eclogites and
104 metasedimentary rocks based on mineral growth zoning and mineral inclusions in garnet (Reinecke
105 1991; van der Klauw et al. 1997). Prograde garnet growth in eclogites lasted for 12 Myr reflecting
106 the duration of slab subduction to UHP conditions at depths >90 km (Lapen et al. 2003). Peak
107 metamorphic conditions reached 615 ± 15 °C and 2.8 ± 1.0 GPa (Reinecke 1991, 1998). Some
108 greenschist-facies retrogression occurs in the eclogites of the LCU (van der Klauw et al. 1997). The
109 peak metamorphic conditions of the LCU overlap with those of eclogite-facies rocks from the

Zermatt-Saas Zone (550-600 °C and 2.5-3.0 GPa). Groppo et al. (2009) have shown that pressure estimates from the meta-ophiolites of the LCU and the Zermatt-Saas Zone differ by less than 0.3 GPa, and both units have identical compositions and zoning patterns of major minerals. Thus, the presence/absence of coesite is the only discriminating factor (Groppo et al. 2009). U-Pb dating of metamorphic zircon and $^{40}Ar/^{39}Ar$ dating of phengite from the LCU gave ages around 44 Ma (Rubatto et al. 1998; Gouzu et al. 2006), similar to those obtained for the Zermatt-Saas zone and hence supporting a similar tectonometamorphic evolution.

Samples

Three samples from the HP/UHP units around Lago di Cignana were investigated (Fig. 2): (1) A fine to medium-grained garnet-phengite quartzite (sample LC-3: 45.8770° N, 7.5933° E) of the LCU contains quartz, garnet and phengite as major mineral phases. The mostly randomly oriented, interlocking or discrete elongated flakes of phengite define a decussate texture. Quartz grains are anhedral with irregular outlines. Euhedral garnet is typically 100-500 μm in diameter and zoned. Typical garnet zoning shows faintly pink coloured cores, relatively enriched in Mn and Mg, and reddish-brownish rims that are richer in Fe and Ca. Minor amphibole and biotite are present, and rutile and opaques occur as accessory phases. (2) A weakly foliated eclogite (sample LC-1b: 45.8786° N, 7.5927° E) from the LCU, which is fine to medium-grained and comprises garnet, omphacite, blue amphibole, epidote, paragonite and quartz as major mineral phases. Euhedral garnet is porphyroblastic and reaches up to 3 mm in diameter. Retrograde chlorite along fractures in garnet is occasionally present but rare, and incipient replacement of blue by green amphibole at the crystal rims is also observed. Accessory phases are rutile and apatite. Paragonite is sometimes associated with rectangular to rhombic outlines of a precursor phase (Fig. 2), which has been interpreted as representing pseudomorphs after lawsonite forming in an early post-peak metamorphic phase during

decompression (Groppo et al., 2009). (3) A strongly foliated, fine-grained metabasite (sample LC-2a: 45.8776° N, 7.5918° E) shows a pervasive retrogression into a greenschist-facies mineral assemblage. This rock belongs to the Zermatt-Saas-Zone and is attributed to the Upper Unit of Groppo et al. (2009). Omphacite, phengite, epidote/clinozoisite, albite and chlorite are the major mineral phases. Amphibole is a minor phase, and titanite and rutile occur as accessory phases.

FIGURE 2 ABOUT HERE

Analytical methods

Wavelength-dispersive quantitative mineral chemical analyses were performed at the University of Kiel (Germany) using a JEOL JXA 8900R electron microprobe. Elements were measured 15 s on peak and 7 s on background with a beam diameter of 5 μm, a beam current of 15 nA and an acceleration voltage of 15 kV. Natural standards were used for calibration and a CITZAF matrix correction was applied. Secondary standards used for quality control were garnet (Roberts Victor 2; USNM 87375), plagioclase (Lake County labradorite; USNM 115900) and olivine (Springwater forsterite 83; USNM 2566) from the Smithsonian Institution, Washington DC (Jarosewich et al. 1980). Element distribution maps were acquired with a Hitachi TM3000 scanning electron microscope at Keele University (see electronic supplementary material).

Boron concentration and isotope analyses were performed at the Edinburgh Ion Microprobe Facility (EIMF) in Edinburgh using a Cameca IMS-1270 ion microprobe. Gold-coated thin sections were sputtered by a 8 nA $^{16}O_2^-$ primary beam with a net impact energy of 22.5 keV in Kohler illumination mode. Sputter pit diameter was ca. 20×30 μm. Mass resolution (ΔM/M) was ~2400 to avoid interferences from $^{9}BeH^+$ and $^{10}BH^+$. At the start of each analysis, the analytical area was pre-sputtered for 60 s using the same beam conditions as during the measurement itself. Subsequently,

using an automated routine, the secondary beam was centred relative to the field aperture and the mass centre of the ^{11}B peak was determined. Each analysis consisted of 50 cycles during which ^{10}B and ^{11}B signals were counted sequentially by an electron multiplier detector with counting times of 8 and 2 s per cycle, respectively. ^{11}B signals were divided by time-averaged ^{10}B signals of the cycles before and after, resulting in 49 $^{11}B/^{10}B$ ratios per analysis. The ^{11}B count rate was ca. 180 cps na^{-1} $\mu g/g^{-1}$. 1s uncertainties are reported in per mil as relative standard error, i.e., the relative standard deviation of all analytical cycles divided by the square root of the total number of cycles. Raw $^{11}B/^{10}B$ ratios were converted to true $^{11}B/^{10}B$ ratios based on reference standards measured at regular intervals throughout the analytical session (see details below) and converted to delta notation ($\delta^{11}B$, per mil deviation from reference standard NIST SRM951) using a value of 4.04362 (Catanzaro et al. 1970). The calibration slope (instrumental mass fractionation) ranged from 0.937 to 0.952 during the session. Boron concentrations were estimated based on ^{11}B count rates of samples and silicate glass reference materials.

The following reference standards were used (Table 1): glasses GOR128-G komatiite and StHs6/80-G dacite (Rosner and Meixner 2004), phengite 80-3 (Pabst et al. 2012), and micas MVE02-8-5 and JJE01-X-3 (Martin et al. 2015). A small offset in $\delta^{11}B$ of -1.2‰ for phengite 80-3 was observed compared to the glasses, in agreement with offset of micas relative to anhydrous glasses reported by Pabst et al. (2012) and De Hoog et al. (2017). Matrix-induced fractionation is often present in SIMS and matrix matching is therefore essential, as the physics behind the fractionation are poorly understood (Eiler et al. 1997, Rosner et al. 2008). Accordingly, mica data reported in this study were also corrected by -1.2‰ relative to the glass standards. Mica MVE02-8-5 has an offset of -4.0‰, which is larger than Phe 80-3, but the published values vary by nearly 3‰, making the material unsuitable for calibration. Mica JJE01-X-3 had a large offset of nearly +7‰ compared to the other two micas, which we cannot explain.

Each set of analyses of the samples was bracketed by 4-6 analyses of basaltic glass GSD1-G and mica

MVE02-8-5 to monitor drift and matrix-dependent fractionation. The remaining glass and mineral standards were measured several times during the analytical session. The precision of the analyses was evaluated as follows: the internal uncertainty was based on the 50 repeat cycles of each analyses, and ranges from 0.3-0.9 ‰ depending on the B concentration of the sample. The drift correction added 0.23% based on the uncertainty of measurements of bracketing standards MVE02-8-5 and GSD1-G, and it presented as external precision in Table 2-4.

The accuracy of the analyses is dependent on the uncertainty of the standards used to determine the matrix-dependent mass fractionation. This uncertainty has two components: the measurement uncertainty and the uncertainty of the literature value. The latter is small for phengite 80-3 (0.35‰; Pabst et al. 2012), but the MVE02-8-5 mica standards suffers from a large uncertainty (1.7 ‰; after Martin et al. 2016) even though our material is homogeneous within counting statistics, suggesting heterogeneity between different batches of the material. In contrast, our phengite 80-3 standard is clearly inhomogeneous, resulting in a relative large uncertainty of 0.9‰ for 7 repeats (Table 1). Nevertheless, the cumulative uncertainty for Phe 80-3 (1.2‰) is much smaller than that of MVE02-8-5, and therefore we only used Phe 80-3 for matrix dependent mass fractionation correction, in line with recent literature (Pabst et al. 2012; Angiboust et al 2014). The uncertainty in the accuracy is presented separately in Tables 2-4, as it is only applicable when comparing our results to B isotope data from the literature.

Results

Mineral chemistry of white mica

The investigated white micas show distinct compositional differences based on Mg# (Mg# = $Mg/[Mg+Fe^{2+}]$), Na/(Na+K) and Si contents (Fig. 3, Tables 2-4; cations calculated on the basis of 22 oxygens). Element distribution maps are provided in the electronic supplementary material.

In the garnet-phengite quartzite (LC-3), the compositional variability of phengite is small with Mg# covering a range from 0.59 to 0.63. Na/(Na+K) ranges from 0.03 to 0.06 and Si per formula unit (p.f.u.) varies between 6.89 and 7.01. Mg# and Si p.f.u. are positively correlated in phengite. Individual phengite grains are homogeneous and do not show any visible zonation in major elements (supplementary Figs. 1 and 2). Adjacent but distinct phengite grains also lack any significant differences in major element composition.

The eclogite (sample LC-1b) contains only paragonite but no phengite, displaying small variations in Na/(Na+K) (0.94 – 0.97) and Si p.f.u. (6.05 – 6.10). Mg# in paragonite is variable, covering a range from 0.54 to 0.75. However, concentrations in both MgO (0.16-0.54 wt%) and FeO (0.18-0.40 wt%) are low, so that small variations in the concentrations have relatively large effects on Mg#. Overall, variations in major element contents are small and element distribution maps show compositionally homogeneous grains (supplementary Fig. 3).

Phengite in the retrogressed metabasite (sample LC-2) is chemically more variable than white mica in the other two samples for both Si p.f.u. (6.67 – 7.03) and Na/(Na+K) (0.04 – 0.12). Mg# varies from 0.76 to 0.90 and correlates positively with Si p.f.u., similar to phengite in the garnet-phengite quartzite. Element distribution maps reveal a patchy zonation in Si, Al and Mg (supplementary Fig. 4). Areas of higher Mg# coincide with elevated Si contents, but the spatial distribution of these areas relative to the grain boundaries is not well defined.

FIGURE 3 ABOUT HERE

Boron elemental and isotopic compositions of white mica

The diagram $\delta^{11}B$ versus B content (Fig. 4) illustrates the key features of boron geochemistry in white mica of the investigated samples (Tables 2-4). Boron concentrations [B] in phengite from the garnet-phengite quartzite (sample LC-3, beige circles) are relatively high compared to the mafic rocks and

range from 109 to 345 μg/g. $\delta^{11}B$ varies from -10.3 to -3.6 ‰, showing a very distinct positive correlation between $\delta^{11}B$ and [B]. Paragonite in the eclogite (sample LC-1b, purple squares) exhibits a range in [B] from 12 to 68 μg/g, with 6 out of 7 analyses yielding <25 μg/g B. $\delta^{11}B$ varies from -5.0 to +2.8 ‰, but a clear correlation between [B] and $\delta^{11}B$ is lacking. Phengite in the retrogressed metabasite (sample LC-2a; blue diamonds) has B contents in the range 29 to 57 μg/g and $\delta^{11}B$ from -4.1 to +3.5. These values show considerable overlap with the B geochemistry of the eclogite (sample LC-1b).

FIGURE 4 ABOUT HERE

Discussion

Effects of protolith geochemistry

Differences in the B contents between white mica from the metabasic rocks (12-68 μg/g B) and the metasedimentary garnet-phengite quartzite (113-345 μg/g B) may reflect the relative B enrichment of sedimentary compared to mafic igneous protoliths. For the metabasic rocks, mafic rocks of the oceanic crust represent protolith lithologies. Boron contents in MORBs range from 0.4 to 2.5 μg/g (Marschall et al. 2017) and whole-rock data for bulk gabbros, dolerites and basalts from the Oman ophiolite vary from <1 to 29 μg/g B (Yamaoka et al. 2012). In comparison, bulk B concentrations in marine sediments are typically higher, ranging from 30 to 120 μg/g in shales (Romer et al. 2014) and from 52 to 100 μg/g in turbidites (Leeman et al. 2004). Siliceous ooze and chert, lithologies that can be taken as potential protoliths to the quartzite, have 35-97 μg/g B (Ishikawa and Nakamura 1993; Kolodny and Chaussidon 2004). Hence, cherts are roughly 10 to 100 times enriched in B compared to typical mafic rocks of the (altered) oceanic crust. Even though the Cignana metabasites are low in K_2O (0.11-0.29 wt.%; Groppo et al. 2009), HP quartzites (1.55 wt.% K_2O; Selverstone and Sharp

2013) are approximately only 10x enriched compared to the metabasites. Therefore, the higher $B_{phengite}$ contents in the garnet-phengite quartzite are consistent with higher [B] in the protolith. Published B concentration data for white mica in metabasic rocks include phengite in blueschist fragments from the Mariana forearc with 29-50 µg/g B (Pabst et al. 2012) as well as phengite and paragonite in metabasic HP rocks from Syros (Greece) with 43-136 µg/g B (Marschall et al. 2006a) and from Guatemala with 0.7-165 µg/g (Martin et al. 2016), overlapping with the values measured in the Lago di Cignana metabasites. In contrast, boron concentrations in white mica from metasedimentary rocks are highly variable but can reach up to 5500 µg/g in continental crustal HP rocks (Sievers et al. 2017).

For potassic white mica, such as phengite, the K_2O content of the bulk rock also influences the B concentration in phengite because phengite is the major host of both K_2O and B in these type of rocks (Bebout and Fogel 1992; Bebout et al. 2007). Therefore, the ratio B/K_2O in phengite is directly proportional to the B/K_2O ratio in the bulk rock. Since K_2O in phengite is essentially fixed to ca. 9-11 wt.% due to crystal chemical controls, protoliths with low K_2O content would crystallize phengite with high B contents as $[B]_{phengite}$ $[B]_{rock}/[K_2O]_{rock}$.

White mica boron geochemistry

Processes that can cause variability in the boron geochemistry of white mica from HP and UHP metamorphic rocks include (1) inhomogeneities of the protolith, (2) retrograde overprint, (3) prograde growth zoning, (4) diffusion, (5) prograde devolatilization with loss of volatile elements, (6) peak metamorphic fluid-rock interaction (Barrientos and Selverstone 1993; Halama and Konrad-Schmolke 2015). In the following, we will first discuss these processes with regard to the garnet-phengite quartzite. For both the eclogite and the retrogressed metabasite, petrographic observations show that white mica formed during retrograde metamorphism, and their boron geochemistry will be evaluated accordingly.

285

286 ***Boron elemental and isotopic systematics in the garnet-phengite quartzite***

287 *(1) Inhomogeneity of the protolith:*

288 Peak metamorphic phengite in the garnet-phengite quartzite has a relatively small range of values for
289 Mg# and Si p.f.u. but highly variable B contents (Fig. 5a, b), suggesting that the boron concentrations
290 in the individual phengite grains are governed by processes that are not reflected in the major element
291 chemistry. Similarly, the $\delta^{11}B$ values vary over seven ‰ without accompanying variation in major
292 elements (Fig. 5c, d), pointing to decoupling of boron isotope variations from major element mineral
293 chemistry. Major element distribution maps also show that adjacent phengite grains are homogenous
294 in their major element chemistry (supplementary Fig. 2). These observations are inconsistent with an
295 inhomogeneous protolith, at least on the thin section scale.

296

297 FIGURE 5 ABOUT HERE

298

299 *(2) Retrograde overprint:*

300 The tight cluster of Si p.f.u. values at 6.95±0.06 and the internal major element homogeneity of
301 individual phengite grains (supplementary Fig. 1) do not support a significant retrograde overprint.
302 The Si content of potassic white mica (muscovite/phengite) is positively correlated with pressure and
303 indicates whether the mineral equilibrated at peak metamorphic conditions or partially recrystallized
304 during a retrograde overprint (Warren et al. 2012), although absolute pressure conditions may only
305 be derived when a limiting assemblage of K-feldspar + phlogopite + quartz (Massonne and Schreyer
306 1987) or garnet + kyanite + qz/cs (Krogh Ravna and Terry 2004) is present. In mineralogically similar
307 garnet-phengite schists from the LCU, phengite inclusions in garnet also have high Si values (6.7 to
308 7.0 p.f.u) reflecting equilibration at UHP conditions, whereas matrix phengites record a much larger
309 chemical variability (6.4 to 7.0 Si p.f.u.), which has been interpreted to reflect retrograde chemical

reactions (Gouzu et al. 2006). The lack of variation in the major element chemistry, the similar textural features of all phengites analysed and the lack of retrograde mineral phases in the garnet-phengite quartzite point to equilibration under identical peak P-T conditions and the lack of any significant influence of a retrograde overprint.

(3) Prograde growth zoning:

Even though the major element composition of the various phengite grains in the garnet-phengite quartzite is relatively homogeneous (supplementary Figs. 1, 2), trace elements may be less homogeneous and can reflect distinct stages of growth zoning. Compositional zoning in trace elements has been shown to reveal complexities in the formation of minerals that were previously undetectable with petrography or major element data since some trace elements are generally less vulnerable to diffusive resetting and can track the mineral reaction history that excludes the major elements (Konrad-Schmolke et al. 2008; Kohn 2014; Raimondo et al. 2017). White mica is able to preserve chemical signatures of their growth history and may even maintain $^{40}Ar/^{39}Ar$ ages reflecting discrete prograde stages of mineral growth (Bröcker et al. 1993; Putliz et al. 2005). Chemical re-equilibration is dominantly controlled by fluid availability and intensity of deformation, and muscovite can partially re-equilibrate without affecting the microstructures (Airaghi et al. 2017). Studies on the behaviour of B in single metamorphic white mica crystals are rare and largely focused on distinct zones that show changes in both major and trace element chemistry related to fluid-induced overprint causing a decrease in B contents (Konrad-Schmolke et al. 2011; Halama et al. 2014). No distinct zonation is observed optically, in back-scattered electron images or in element distribution maps in phengites from sample LC-3. Moreover, the analysis spots in the different phengite crystals are all in a central position in grains with similar texture and major element chemistry (Fig. 6). Therefore, there is no indication of growth zoning in phengite.

FIGURE 6 ABOUT HERE

335

336 *(4) Diffusion:*

337 For boron, only very few studies have evaluated high-temperature diffusion-induced B isotope
338 fractionation (Kowalski and Wunder 2018). Experimental data show that kinetic B isotope
339 fractionation is insignificant at melt crystallization temperatures (1200-1600 °C; Chakraborty et al.
340 1993). In natural samples, B abundances in mantle xenolith minerals do not vary significantly,
341 consistent with expected low B diffusivities (Kaliwoda et al. 2008), and uniform compositions in
342 deformed and undeformed tourmaline also indicate the absence of significant B diffusion (Büttner
343 and Kasemann 2007). Hence, in accordance with Kowalski and Wunder (2018), B isotope
344 fractionation from diffusion is not considered here.

345 *(5) Prograde devolatilization*:

346 Zoning in both [B] and δ^{11}B has been studied extensively in metamorphic tourmaline. For instance,
347 zoned tourmalines in metasedimentary rocks show decreasing δ^{11}B values from core to rim (Nakano
348 and Nakamura 2001; Bebout and Nakamura 2003; Berryman et al. 2017). This core-to-rim zoning
349 pattern is thought to reflect progressive devolatilization of B during metamorphism (Bebout and
350 Nakamura 2003). Boron originally present in white mica is mobilized into a fluid phase with ^{11}B
351 preferentially removed from the rock during prograde dehydration (Wunder et al. 2005). This results
352 in a trend to lower δ^{11}B values in mica and fluid, which is reflected in concurrently growing
353 tourmaline (Bebout and Nakamura 2003; Berryman et al. 2017). The loss of B from white mica during
354 prograde metamorphism and progressive devolatilization will lead to the formation of mica with more
355 negative δ^{11}B values.

356 Here, we test whether the B systematics in the garnet-phengite quartzite reflect devolatilization of B
357 during metamorphism. We test this model by a Rayleigh distillation calculation, using the formula

358

359 where $\delta^{11}B_f$ and $\delta^{11}B_i$ are the final and initial B isotopic compositions of the rock, F is the fraction of

360 B that remains in the rock after devolatilization, and α is the temperature-dependent fluid-mineral
361 fractionation factor (Wunder et al. 2005). For the fluid-phengite fractionation factor, we use a value
362 of 1.00833 reflecting a temperature of 600 °C. The other parameters that need to be constrained for
363 the modelling are the initial B contents and $\delta^{11}B$ values. We calculated two curves based on initial
364 $\delta^{11}B$ values of -4 ‰ and +2 ‰ and 400 µg/g B. However, higher initial values for both B and $\delta^{11}B$
365 are also permitted by the data. For instance, a combination of B = 750 µg/g and $\delta^{11}B$ = +4 ‰ would
366 produce a devolatilization curve that fits the data points in a manner similar to the curves described
367 above (Fig. 7).
368 The modelled fraction of B lost during devolatilization depends on the initial B content and $\delta^{11}B$
369 value, both of which are unconstrained. The assumed initial B contents in phengite can be related to
370 whole rock [B] by using the relationship $(B/K_2O)_{phe} = (B/K_2O)_{WR}$, where $[K_2O]_{phe}$ = 10 wt.% and
371 $[K_2O]_{WR}$ is assumed to be 1.55 wt.% (Selverstone and Sharp 2013). Then, [B] content would vary
372 between 60 and 116 µg/g, which overlaps with measured values for siliceous sedimentary rocks. We
373 can also evaluate the unknown initial $\delta^{11}B$ of the protolith by comparison with published data on
374 sedimentary rocks. These cover a range of >30 ‰, from $\delta^{11}B$ = -24 to +5 ‰ (Ishikawa and Nakamura
375 1993; Leeman et al. 2004; Romer et al. 2014; Tonarini et al. 2011). This considerable range of
376 potential initial isotopic ratios in the protolith is problematic for assigning accurate initial parameters
377 for modelling any kind of fluid-rock interaction (Romer et al. 2014). Restricting the protolith to
378 known silica-rich rock compositions (siliceous ooze and chert) provides only a small limitation, as
379 values vary from -17.0 to +8 ‰ (Ishikawa and Nakamura 1993; Kolodny and Chaussidon 2004). We
380 note, however, that high positive values ($\delta^{11}B$ > 4 ‰) are rare and most values fall between -8 and
381 +4 ‰, suggesting that an initial starting point of $\delta^{11}B$ = +4 ‰ serves as a reasonable upper limit.
382 Model curves based on more extreme initial mica compositions (e.g. B = 1400 µg/g and $\delta^{11}B$ =
383 +10 ‰) that also fit the data are therefore excluded.
384 The modelling of the phengite composition in the garnet-phengite quartzite indicates a loss of 15-

385 75 % B for an initial composition of 400 µg/g B and $\delta^{11}B = 0\pm2$ ‰, and a loss of 55-85% B if initial
386 values of 750 µg/g B and $\delta^{11}B = +4$ ‰ are assumed (Fig. 7). For both modelled scenarios, the wide
387 range of B contents and $\delta^{11}B$ values in phengite is noteworthy, as this pattern in different whole rock
388 samples would suggest different degrees of devolatilization due to different temperatures reached. In
389 a single, well-equilibrated sample that contains chemically (Fig. 3) and texturally (Fig. 6)
390 indistinguishable phengites, this explanation is untenable. The analysed spots are in mica grains of
391 similar size with random orientations, and measurements were typically taken in central parts of the
392 grain. There is no obvious relationship of [B] or $\delta^{11}B$ with spot position or grain orientation (Fig. 6).
393 Preservation of initial differences in B content of the individual phengite grains cannot be entirely
394 excluded, but it does not seem to be a major factor based on the only small variations in all other
395 mineral chemical parameters and the intra-grain and inter-grain major element homogeneity
396 (supplementary Figs. 1, 2). Despite the good model fit to the data, the implicit large variations in
397 devolatilization efficiency are unrealistically high and do not support the devolatilization model.
398
399 FIGURE 7 ABOUT HERE
400
401 *(6) Peak metamorphic fluid-rock interaction*
402 Since none of the processes discussed above satisfactorily explains the petrographic observations in
403 combination with the variable [B]-$\delta^{11}B$ data, we will now evaluate whether fluid-rock interaction
404 with an intergranular fluid phase at or near peak-metamorphic conditions can provide an answer. If
405 such a model can be conceptually applied to the garnet-phengite quartzite, it implies that the fluid did
406 not interact with all individual phengites to the same degree. Instead, some phengites retained their
407 initial or near-initial B geochemical signatures, whereas other phengite grains were able to exchange
408 B with the fluid for an extended period, leading to significant modifications in both [B] and $\delta^{11}B$.
409 Variations in both [B] and $\delta^{11}B$ have been extensively studied in metamorphic tourmaline, where the

involvement of distinct fluids with distinct B isotope composition was used to explain tourmaline rims that are either lighter (Trumbull et al. 2009) or heavier (Marschall et al. 2008) than the respective cores during open system tourmaline crystallization.

For the fluid-rock interaction modelling, we use equations for open system fluid-rock interaction presented in Nabelek (1987). For B concentrations, the fluid/rock ratio *N* is determined as:

—

where is the final concentration of the trace element in the rock, is the initial trace element concentration in the rock, is the initial trace element concentration in the fluid, *D* is the partition coefficient between fluid and rock. This equation is solved for :

—

For the boron partition coefficient between fluid and white mica, we use a value of 1.4 based on the work by Marschall et al. (2006a). The parameters and are adjusted to obtain a reasonable fit for the model curves. Stable B isotope exchange is modelled using an equation from Taylor (1977),

where *N* is the fluid/rock ratio, is the initial stable isotope ratio in the fluid, is the initial stable isotope ratio in the rock, is the final stable isotope ratio in the rock, and Δ is the equilibrium stable isotope fractionation between rocks and fluid ($\Delta = \delta_r - \delta_w$). This equation is solved for :

We assume a temperature of 600 °C for the peak metamorphic fluid-rock interaction, which results in a $\Delta^{11}B$ of -8.4 ‰ for neutral and acidic fluids (Wunder et al. 2005). The parameters and were varied, and eventually the open system exchange equations for the trace element B and the B isotope composition were combined.

Two distinct scenarios of fluid-rock interaction are considered, assuming a temperature of 600 °C that is appropriate for peak metamorphic conditions (Fig. 8). In the first case, white mica is assumed to lose B, leading to successively lower $\delta^{11}B$ values with increasing *N* (Fig. 8a). In the second case, white mica is assumed to gain B from a B-rich fluid (Fig. 8b). Fluid-rock interaction modelling provides suitable solutions for both scenarios, suggesting that it is an appropriate process to explain the [B]-$\delta^{11}B$ variability in white mica. Since both modelled scenarios of fluid-rock interaction fit the data using appropriate parameters, the models themselves cannot distinguish which scenario is more likely. The models show that low fluid/rock ratios (≤ 1) are sufficient to cause significant variation in B concentration and B isotopic composition. Importantly, a scenario of small amount of intergranular fluid interaction with the rocks at (ultra)high pressures is consistent with the petrographic and textural evidence.

The range of parameters chosen to obtain a good model fit provide an indication about the likely fluid composition. For the first case (boron leaching; Fig. 8a), the initial fluid composition is approximately constrained to $\delta^{11}B_{fluid}$ = -7±3 ‰ and [B] = 10-40 µg/g, using initial values for white mica of [B] = 500-750 µg/g and $\delta^{11}B_{mica}$ = +2±4 ‰ (Fig. 8a). These highly negative $\delta^{11}B_{fluid}$ values imply residual rock compositions with even more negative $\delta^{11}B$ values around -12 to -18 ‰ (at 600 °C) from which these fluids were derived. Such low $\delta^{11}B$ values are at the lower end of $\delta^{11}B$ values that have been observed in high-pressure metamorphic rocks, which typically range from -15 to +5 ‰ (Peacock and Hervig 1999; Nakano and Nakamura 2001; Pabst et al. 2012; Angiboust et al. 2014; Halama et al., 2014). If these values were reached in the subducting slab, near-complete preceding devolatilization would be required, leaving little fluid around to potentially interact with surrounding rocks.

In the second case (boron addition; Fig. 8b), a B-rich fluid with high positive $\delta^{11}B$ values ($\delta^{11}B$ = +20±5) can constrain fluid-rock interaction models that encompass the data points. All of these boron addition models require only small fluid/rock ratios (≤0.6). High positive $\delta^{11}B$ values are typical for

457 slab serpentinites that formed by subduction fluid infiltration, covering a wide range in $\delta^{11}B$ from +7
458 to +24 (Scambelluri and Tonarini 2012). Isotopic fractionation between serpentine and fluid is not
459 well constrained, but minimal fractionation is expected if the pH value of the fluid is high and only
460 at lower pH values would the fluid become isotopically lighter than the serpentinite (Benton et al.
461 2001), corresponding to a more positive $\delta^{11}B$ in the fluid source rocks. However, serpentine
462 dehydrates over a small temperature interval so that all fluid released is likely to be pooled and would
463 then have the same B isotopic composition as the serpentine. Hence, the range of modelled $\delta^{11}B_{fluid}$
464 values is in good agreement with serpentinite as fluid source rock. The high B contents are more
465 problematic to explain, but high B contents (250 mg/l) were reported from fluids interpreted to reflect
466 slab dehydration (Boschetti et al. 2017) and determined in melt inclusions (up to ca. 200 µg/g) thought
467 to reflect a slab fluid influence (Jones et al., 2014). Serpentine minerals often have high B
468 concentrations, typically around 10-100 µg/g (Benton et al. 2001; Vils et al. 2008), which makes them
469 a suitable source for high-B fluids. Thermodynamic-geochemical modelling also suggest that
470 breakdown of serpentine during subduction can release B-rich, high-$\delta^{11}B$ fluids (Konrad-Schmolke
471 and Halama 2014; Konrad-Schmolke et al. 2016). Moreover, the scenario of serpentinite-derived
472 fluids fits with the Cignana peak P-T metamorphic conditions, which are similar to the expected
473 antigorite breakdown (ca. 600-650 °C; Padrón-Navarta et al. 2013) and the abundant presence of
474 serpentinites in the area. Hence, fluid-rock interaction at peak metamorphic conditions successfully
475 explains the [B]-$\delta^{11}B$ relationships, and serpentinite-derived fluid represents a likely candidate to
476 account for this process. This interpretation implies that the fluid did not interact with all phengites
477 to the same degree, but cause variable exchange of B with the fluid for different periods of time,
478 leading to the observed variations.
479
480 FIGURE 8 ABOUT HERE
481

482 ***Fluid-rock interaction during retrograde metamorphism***

483 In both the eclogite and the retrogressed metabasite, white mica formed during post-peak
484 metamorphic conditions. The breakdown of lawsonite, which is observed in the eclogite, is commonly
485 caused by pressure decrease and/or temperature increase (Heinrich and Althaus 1988). For eclogites
486 from Lago di Cignana, Groppo et al. (2009) concluded based on detailed petrographic observations
487 and pseudosection modelling that lawsonite was part of the peak metamorphic assemblage and
488 breakdown of lawsonite to epidote + paragonite occurred during decompression, reflecting a
489 retrograde post-peak metamorphic assemblage. The paragonite in the eclogite has constant Si but
490 variable Mg# (Fig. 5), suggesting equilibration with somewhat different proportions of neighbouring
491 minerals during replacement of lawsonite and hence different effective bulk compositions of the
492 equilibrated rock volume. However, intra-grain variability in major element composition is small and
493 no clear zonation is discernible in element distribution maps (supplementary Fig. 3). Ion microprobe
494 analysis spots were placed in central parts of texturally similar mica grains, so that any obvious
495 influence of texture/position on the B geochemistry was avoided.
496 Phengite in the retrogressed metabasite is variable in both Mg# and Si p.f.u., indicating variable and
497 extended recrystallization on the retrograde P-T path. The weak patchy zonation in Si, Al and Mg
498 suggests only partial re-equilibration during retrogression leading to the preservation of chemically
499 distinct mica domains (supplementary Fig. 4). A more variable chemical composition in secondary
500 white mica that formed due to retrograde reactions compared to homogeneous primary, peak
501 metamorphic white mica has been also observed in a subduction-related HP metagabbro that
502 preserves an eclogite-facies assemblage (Putlitz et al. 2005). $\delta^{11}B$ in phengite shows a weak positive
503 correlation with Mg# and Si, but a clear correlation of [B] with major element chemical parameters
504 is absent.
505 Both rocks had a mafic igneous rock as protolith. They also reached similar peak P-T conditions, but
506 given the effects of retrograde metamorphism it is unlikely that effects of prograde and peak

metamorphic processes are recorded in the [B]-$\delta^{11}B$ systematics. For instance, the lack of a systematic correlation between [B] and $\delta^{11}B$ (Fig. 4) and the large spread in $\delta^{11}B$ values (ca. 9 ‰) over a small interval in [B] are difficult to reconcile with devolatilization trends or prograde zonation. Instead, we will test and model the effects of fluid-rock interaction on the B systematic of these rocks, using the equations presented earlier in the text.

We assume a temperature of 400 °C for the retrograde overprint, which results in a $\Delta^{11}B$ of -12.0 ‰ for neutral and acidic fluids (Wunder et al. 2005). The parameters and were varied, and eventually the open system exchange equations for the trace element B and the B isotope composition were combined. The B partition coefficients for fluid/phengite (1.4) and fluid/paragonite (0.9) are slightly different (Marschall et al. 2006a). They are derived from a combination of clinopyroxene/fluid partition coefficients (Brenan et al. 1998) and inter-mineral partition coefficients (Marschall et al. 2006a). The relative uncertainties in these inter-mineral partition coefficients are ~39% for clinopyroxene/phengite (0.0026 ± 0.010, n=5) and ~22% for clinopyroxene/paragonite (0.015 ± 0.003, n=2), respectively. Assuming an overall relative uncertainty of 40% for fluid/mica partition coefficients, values for fluid/phengite and fluid/paragonite overlap and for clarity all models were calculated using the fluid/phengite partition coefficient. The model curves shown (Fig. 9) encompass all data points. As for the garnet-phengite quartzite, two different sets of models were developed.

The initial fluid composition in the first set of models, reflecting boron leaching (Fig. 9a), can be approximated as $\delta^{11}B_{fluid}$ = +6±6 ‰ and [B] = 5 µg/g. With these parameters, the data can be successfully modelled for values of N ranging from ~0.2 to ~3. The second set of models, reflecting addition of boron (Fig. 9b), constrains the initial fluid to very high $\delta^{11}B$ values (+14 to +32) with high B contents of 200-400 µg/g (Fig. 9b). All data points can be explained with low fluid/rock ratios (N <0.5).

The [B]-$\delta^{11}B$ systematics in white mica from the Catalina Schist were linked to fluids from highly

532 devolatilized (low $\delta^{11}B$) and less devolatilized (moderate $\delta^{11}B$ of -2 to +8 ‰) rocks (Sievers et al.
533 2017). Depletion of B during fluid-rock interaction has also been observed in the HP rocks from the
534 Sesia zone where a percolating fluid caused a decrease in [B] in overprinted phengite rims (Konrad-
535 Schmolke et al. 2011; Halama et al. 2014). The range in $\delta^{11}B$ for the shallow fluids from moderately
536 devolatilized rocks overlaps well with the initial $\delta^{11}B_{fluid}$ in the first set of model calculations. King
537 et al. (2007) proposed a range in $\delta^{11}B$ between +2 ‰ at 500 °C and +9 ‰ at 300 °C for slab-derived
538 fluids, overlapping the B isotopic compositions of the fluids in our models (Fig. 9a). Tourmalines
539 from Lago di Cignana metasedimentary rocks show an increase of $\delta^{11}B$ values to +4 ‰, which
540 resulted from retrograde influx of B by fluids (Bebout and Nakamura 2003). Since the B isotope
541 fractionation between tourmaline and fluid is relatively small ($\Delta^{11}B_{tourmaline\text{-}fluid}$ = -2.7 ‰ at 400 °C;
542 Meyer et al. 2008), these tourmaline $\delta^{11}B$ values correspond to $\delta^{11}B_{fluid}$ values of around +7, in perfect
543 agreement with our modelled fluid compositions (Fig. 9a). In contrast, the second set of calculations
544 (Fig. 9b) requires at residual rocks with highly positive $\delta^{11}B$, which would be in line with a
545 serpentinite-derived fluid but not with fluids derived from typical metabasites or metapelites.
546 Serpentinites, however, are dehydrating at temperatures above 600 °C on the prograde metamorphic
547 path, so it is difficult to envisage how serpentinite would be able to release fluid on the retrograde
548 path. Therefore, the boron addition model does not seem feasible for the retrograde white mica, and
549 instead boron leaching from the rocks is our preferred interpretation.
550 The key observation derived from the modelling is that small to moderate fluid/rock ratios are
551 sufficient to cause significant shifts in [B] and the moderate decrease in $\delta^{11}B_{mica}$. This remains true
552 even when the significant uncertainties in some of the variables are taken into account. Rather than
553 putting too much weight on the uncertainties in the model parameters it is worth emphasizing that the
554 general process of fluid-rock interaction is suitable to explain the B geochemistry systematics of white
555 mica in retrograde overprinted (U)HP metamorphic rocks and consistent with the petrographic and
556 petrologic constraints. We therefore suggest that retrograde white mica and tourmaline rims record a

similar overprint by the same kind of fluids.

FIGURE 9 ABOUT HERE

Conclusions

The white mica B concentration and isotopic data of the three Lago di Cignana (U)HP samples that have experienced a similar P/T evolution in a subduction zone setting reveal significant variability both between and within the samples. Phengite in a metasedimentary garnet-phengite quartzite has the highest B contents, reflecting B enrichment coupled too low to moderate K_2O contents in the siliceous protolith. The decrease in $\delta^{11}B$ with decreasing [B] cannot be explained by textural differences between grains, prograde growth zoning, diffusion or retrogression. The trend can be successfully modelled using a Rayleigh distillation equation, simulating devolatilization of B during prograde metamorphism, but this process fails to explain the wide range in [B] and $\delta^{11}B$ in well-equilibrated rocks with a population of petrographically and texturally indistinguishable phengite. Alternatively, we modelled fluid-rock interaction at peak metamorphic conditions and several models successfully mirror the arrangement of data points. Our preferred model invokes fluid-rock interaction with a serpentinite-derived, high-B, high-$\delta^{11}B$ ($\delta^{11}B = +20\pm5$) fluid at or near peak metamorphic conditions. The [B]-$\delta^{11}B$ variations in two samples that show a clear retrograde metamorphic overprint can be modelled by fluid-rock interaction at low to moderate (<3) fluid/rock ratios during retrogression. The modelled fluid composition yields a moderately positive $\delta^{11}B$ of $+6\pm6$, which agrees well with slab-derived fluids generally and those for Lago di Cignana in particular. Our observations underline the value of *in situ* observations of fluid-rock interaction processes in HP metamorphic rocks, which in turn is crucial for our understanding of the links between metamorphic processes in subduction zones and the geochemistry of arc magmatic rocks.

582

583

584 ## Acknowledgments

585 We thank P. Appel and B. Mader (Kiel University) for help with electron microprobe work and D.
586 Wilde (Keele University) for thin section preparation. We also thank the organizers of the 10th
587 International Eclogite Conference for the excellent introduction to the Lago di Cignana area.
588 Constructive comments by C. Martin and an anonymous reviewer helped to improve the manuscript
589 and are greatly appreciated. D. Rubatto is thanked for editorial handling of the manuscript. Funding
590 for ion microprobe analyses through NERC IMF grant 602/1016 to RH is gratefully acknowledged.

591 # References

592

593 Airaghi L, Lanari P, de Sigoyer J, Guillot S (2017) Microstructural vs compositional preservation and
594 pseudomorphic replacement of muscovite in deformed metapelites from the Longmen Shan (Sichuan,
595 China). Lithos 282-283:262-280.

596

597 Angiboust S, Pettke T, De Hoog JCM, Caron B, Oncken O (2014) Channelized fluid flow and
598 eclogite-facies metasomatism along the subduction shear zone. J Petrol 55:883-916.

599

600 Barrientos X, Selverstone J (1993) Infiltration vs. thermal overprinting of epidote blueschist, Ile de
601 Groix, France. Geology 21:69–72.

602

603 Bearth P. (1967) Die Ophiolithe der Zone von Zermatt-Saas Fee. Beiträge zur Geologischen Karte
604 der Schweiz, N.F., 132, 130 p.

605

606 Bebout GE, Bebout AE, Graham CM (2007). Cycling of B, Li, and LILE (K, Cs, Rb, Ba, Sr) into
607 subduction zones: SIMS evidence from micas in high-P/T metasedimentary rocks. Chem Geol
608 239:284-304.

609

610 Bebout GE, Fogel M (1992) Nitrogen-isotope compositions of metasedimentary rocks in the Catalina
611 Schist, California: Implications for metamorphic devolatilization history. Geochim Cosmochim Acta
612 56:2839-2849.

613

614 Bebout GE, Nakamura E (2003) Record in metamorphic tourmalines of subduction-zone
615 devolatilization and boron cycling. Geology 31:407–410.

Bebout GE, Ryan JG, Leeman WP, Bebout AE (1999) Fractionation of trace elements by subduction-zone metamorphism – effect of convergent-margin thermal evolution. Earth Planet Sci Lett 171:63-81.

Beltrando M, Compagnoni R, Lombardo B (2010) (Ultra-) High-pressure metamorphism and orogenesis: An Alpine perspective. Gondwana Res 18:147-166.

Beltrando M, Lister G, Forster M, Dunlap WJ, Fraser G, Hermann J (2009) Dating microstructures by the ^{40}Ar-^{39}Ar step-heating technique: deformation-Pressure-Temperature-time history of the Penninic Units of the Western Alps. Lithos 113:801-819.

Benton LD, Ryan JG, Tera F (2001) Boron isotope systematics of slab fluids as inferred from a serpentine seamount, Mariana forearc. Earth Planet Sci Lett 187:273-282.

Berryman EJ, Kutzschbach M, Trumbull RB, Meixner A, van Hinsberg V, Kasemann SA, Franz G (2017). Tourmaline as a petrogenetic indicator in the Pfitsch Formation, Western Tauern Window, Eastern Alps. Lithos 284-285:138-155.

Boschetti T, Toscani L, Iacumin P, Selmo E (2017). Oxygen, Hydrogen, Boron and Lithium Isotope Data of a Natural Spring Water with an Extreme Composition: A Fluid from the Dehydrating Slab? Aquat Geochem 23:299-313.

Brenan JM, Ryerson FJ, Shaw HF (1998). The role of aqueous fluids in the slab-to-mantle transfer of boron, beryllium, and lithium during subduction: experiments and models. Geochim Cosmochim

641 Acta 62:3337–3347.
642
643 Bröcker M, Kreuzer H, Matthews A, Okrusch M (1993). $^{40}Ar/^{39}Ar$ and oxygen istopes studies of
644 polymetamorphism from Tinos island, Cycladic blueschist belt, Greece. J metamorph Geol 11:223–
645 240.
646
647 Büttner SH, Kasemann S (2007) Deformation-controlled cation diffusion in tourmaline: A
648 microanalytical study on trace elements and boron isotopes. Am Mineral 92:1862-1874.
649
650 Catanzaro FJ, Champion CE, Garner EL, Marinenko G, Sappenfield KM, Shields WR (1970) Boric
651 acid: isotopic and assay standard reference materials. Natl Bur Stand Spec Publ 260:1–70.
652
653 Chakraborty S, Dingwell D, Chaussidon M (1993) Chemical diffusivity of boron in melts of
654 haplogranitic composition. Geochim Cosmochim Acta 57:1741-1751.
655
656 Compagnoni R, Rolfo R (2003) UHPM units in the Western Alps. In: Carswell DA, Compagnoni R
657 (eds.) Ultrahigh Pressure Metamorphism, EMU Notes in Mineralogy, Eötvös University Press,
658 Budapest, vol 5, pp 13-49.
659
660 Dal Piaz GV (1974) Le métamorphisme de haute pression et basse température dans l'évolution
661 structurale du basin ophiolitique alpino-apenninique. Schweiz Mineral Petrogr Mitt 54:399–424.
662
663 Dal Piaz GV, Di Battistini G, Kienast JR, Venturelli G (1979) Manganiferous quartzitic schists of the
664 Piemonte ophiolite nappe in the Valsesia-Valtournanche area (Italian Western Alps). Mem Sci Geol
665 Padova 32:1–24.

De Hoog JCM, Monteleone B, Savov IP, Marschall HR, Zack T, EIMF (2017) Matrix effects in B isotope analysis of silicate minerals by SIMS. Goldschmidt Conference Abstract #872, Goldschmidt Conference, Paris, August 13-18, 2017.

De Hoog JCM, Savov IP (2018) Boron isotopes as a tracer of subduction zone processes. In: Marschall H, Foster G (eds) Boron Isotopes, Advances in Isotope Geochemistry, Springer International Publishing, chapter 9, pp 217-247.

Eiler JM, Graham C, Valley JW (1997) SIMS analysis of oxygen isotopes: Matrix effects in complex minerals and glasses. Chemical Geology 138:221–244.

Frezzotti, ML, Huizenga JM, Compagnoni R, Selverstone J (2014) Diamond formation by carbon saturation in C–O–H fluids during cold subduction of oceanic lithosphere. Geochim Cosmochim Acta 143:68–86.

Frezzotti ML, Selverstone J, Sharp ZD, Compagnoni R (2011) Carbonate dissolution during subduction revealed by diamond-bearing rocks from the Alps. Nat Geosci 4:703–706.

Gouzu C, Itaya T, Hyodo H, Matsuda T (2006) Excess ^{40}Ar-free phengite in ultrahigh-pressure metamorphic rocks from the Lago di Cignana area, Western Alps. Lithos 92:418–430.

Groppo C, Beltrando M, Compagnoni R (2009) P–T path of the UHP Lago di Cignana and adjoining HP meta-ophiolitic units: insights into the evolution of the subducting Tethyan slab. J metamorph Geol 27:207–231.

691

692 Halama R, Konrad-Schmolke M (2015) Retrograde metasomatic effects on phase assemblages in an
693 interlayered blueschist–greenschist sequence (Coastal Cordillera, Chile). Lithos 216-217:31-47.
694

695 Halama R, Konrad-Schmolke M, Sudo M, Marschall HR, Wiedenbeck M (2014) Effects of fluid–
696 rock interaction on $^{40}Ar/^{39}Ar$ geochronology in high-pressure rocks (Sesia-Lanzo Zone, Western
697 Alps). Geochim Cosmochim Acta 126:475-494.
698

699 Heinrich W, Althaus E (1988) Experimental determination of the reaction 4 lawsonite + 1 albite = 1
700 paragonite + 2 zoisite + 2 quartz + 6 H_2O and 4 lawsonite + 1 jadeite = 1 paragonite + 2 zoisite + 1
701 quartz + 6 H_2O. Neues Jahrbuch für Mineralogie Monatshefte 11:516-528.
702

703 Ishikawa T, Nakamura E (1993) Boron isotope systematics of marine sediments. Earth Planet Sci
704 Lett 117:567-580.
705

706 Ishikawa T, Nakamura E (1994) Origin of the slab component in arc lavas from across-arc variation
707 of B and Pb isotopes. Nature 370:205–208.
708

709 Ishikawa T, Tera F, Nakazawa T (2001) Boron isotope and trace element systematics of the three
710 volcanic zones in the Kamchatka arc. Geochim Cosmochim Acta 65:4523–4537.
711

712 Jarosewich E, Nelen JA, Norbers JA (1980) Reference samples for electron microprobe analysis.
713 Geostandards Newsletter 4:43-47.
714

715 Jochum KP, Wilson SA, Abouchami W, Amini M, Chmeleff J, Eisenhauer A, Hegner E, Iaccheri

716 LM, Kieffer B, Krause J, McDonough WF, Mertz-Kraus R, Raczek I, Rudnick RL, Scholz D,
717 Steinhoefel G, Stoll B, Stracke A, Tonarini S, Weis D, Weis U, Woodhead JD (2011) GSD-1G and
718 MPI-DING Reference Glasses for In Situ and Bulk Isotopic Determination. Geostandards and
719 Geoanalytical Research 35:193-226.
720
721 Jones RE, De Hoog JCM, Kirstein LA, Kasemann SA, Hinton R, Elliott T, Litvak VD, EIMF (2014).
722 Temporal variations in the influence of the subducting slab on Central Andean arc magmas: Evidence
723 from boron isotope systematics. Earth Planet Sci Lett 408:390-401.
724
725 Kaliwoda M, Ludwig T, Altherr R (2008) A new SIMS study of Li, Be, B and δ^7Li in mantle xenoliths
726 from Harrat Uwayrid (Saudi Arabia). Lithos 106:261-279.
727
728 King RL, Bebout GE, Grove M, Moriguti T, Nakamura E (2007) Boron and lead isotope signatures
729 of subduction-zone mélange formation: Hybridization and fractionation along the slab–mantle
730 interface beneath volcanic arcs. Chem Geol 239:305-322.
731
732 Kohn MJ (2014) Geochemical zoning in metamorphic minerals. In: Rudnick, RL (ed.), Treatise on
733 Geochemistry: The Crust, 4, pp 249-280.
734
735 Kolodny Y, Chaussidon M (2004) Boron isotopes in DSDP cherts: fractionation and diagenesis.
736 Geochem Soc Spec Publ 9:1-14.
737
738 Konrad-Schmolke M, Halama R (2014). Combined thermodynamic-geochemical modeling in
739 metamorphic geology: Boron as tracer of fluid-rock interaction. Lithos 208:393-414.
740

741 Konrad-Schmolke M, Halama R, Manea VC (2016) Slab mantle dehydrates beneath Kamchatka –
742 yet recycles water into the deep mantle. Geochem Geophys Geosyst 17.
743 https://doi:10.1002/2016GC006335.
744
745 Konrad-Schmolke M, Zack T, O'Brien P, Barth M (2011) Fluid migration above a subducted slab –
746 thermodynamic and trace element modelling of fluid–rock interaction in partially overprinted
747 eclogite-facies rocks (Sesia Zone, Western Alps). Earth Planet Sci Lett 311:287–298.
748
749 Konrad-Schmolke M, Zack T, O'Brien PJ, Jacob D (2008) Combined thermodynamic and rare earth
750 element modelling of garnet growth during subduction: Examples from ultrahigh-pressure eclogite
751 of the Western Gneiss Region, Norway. Earth Planet Sci Lett 272:488-498.
752
753 Kowalski PM, Wunder B (2018) Boron isotope fractionation among vapour-liquids-solids-melts:
754 Experiments and atomistic modeling. In: Marschall H, Foster G (eds.) Boron Isotopes, Advances in
755 Isotope Geochemistry, Springer International Publishing, chapter 3, pp 33-69.
756
757 Krogh Ravna EJ, Terry MP (2004) Geothermobarometry of UHP and HP eclogites and schists – an
758 evaluation of equilibria among garnet-clinopyroxene-kyanite-phengite-coesite/quartz. J metamorph
759 Geol 22:579-592.
760
761 Lapen TJ, Johnson CM, Baumgartner LP, Mahlen NJ, Beard BL, Amato JM (2003) Burial rates
762 during prograde metamorphism of an ultra-high-pressure terrane: an example from Lago di Cignana,
763 western Alps, Italy. Earth Planet Sci Lett 215:57–72.
764
765 Leeman WP, Tonarini S, Chan LH, Borg LE (2004) Boron and lithium isotopic variations in a hot

766 subduction zone – the southern Washington Cascades. Chem Geol 212:101-124.
767
768 Marschall HR, Altherr R, Gméling K, Kasztovszky Z (2009) Lithium, boron and chlorine as tracers
769 for metasomatism in high-pressure metamorphic rocks: a case study from Syros (Greece). Mineral
770 Petrol 95:291–302.
771
772 Marschall HR, Altherr R, Kalt A, Ludwig T (2008) Detrital, metamorphic and metasomatic
773 tourmaline in high-pressure metasediments from Syros (Greece): intra-grain boron isotope patterns
774 determined by secondary-ion mass spectrometry. Contrib Mineral Petrol 155:703-717.
775
776 Marschall HR, Altherr R, Ludwig T, Kalt A, Gméling K, Kasztovszky Z (2006a) Partitioning and
777 budget of Li, Be and B in high-pressure metamorphic rocks. Geochim Cosmochim Acta 70:4750-
778 4769.
779
780 Marschall HR, Altherr R, Rüpke L (2007) Squeezing out the slab—modelling the release of Li, Be
781 and B during progressive high-pressure metamorphism. Chem Geol 239:323–335.
782
783 Marschall HR, Ludwig T, Altherr R, Kalt A, Tonarini S (2006b) Syros metasomatic tourmaline:
784 Evidence for very high-δ^{11}B fluids in subduction zones. J Petrol 47:1915-1942.
785
786 Marschall HR, Wanless VD, Shimizu N, Pogge von Strandmann PAE, Elliott T, Monteleone B (2017)
787 The boron and lithium isotopic composition of mid-ocean ridge basalts and the mantle. Geochim
788 Cosmochim Acta 207:102-138.
789
790 Martin C, Flores KE, Harlow GE (2016) Boron isotopic discrimination for subduction-related

791 serpentinites. Geology 44:899-902.
792
793 Martin C, Ponzevera E, Harlow G (2015) In situ lithium and boron isotope determinations in mica,
794 pyroxene, and serpentine by LA-MC-ICP-MS. Chem Geol 412:107-116.
795
796 Massonne HU, Schreyer W (1987) Phengite geobarometry based on the limiting assemblage with K-
797 feldspar, phlogopite, and quartz. Contrib Mineral Petrol 96:212–224.
798
799 Meyer C, Wunder B, Meixner A, Romer RL, Heinrich W (2008) Boron-isotope fractionation between
800 tourmaline and fluid: an experimental re-investigation. Contrib Mineral Petrol 156:259-267.
801
802 Moran AE, Sisson VB, Leeman WP (1992) Boron depletion during progressive metamorphism:
803 implications for subduction processes. Earth Planet Sci Lett 111:331–349.
804
805 Nabelek PI (1987) General equations for modelling fluid/rock interaction using trace elements and
806 isotopes. Geochim Cosmochim Acta 51:1765-1769.
807
808 Nakano T, Nakamura E (2001) Boron isotope geochemistry of metasedimentary rocks and
809 tourmalines in a subduction zone metamorphic suite. Phys Earth Planet Inter 127:233–252.
810
811 Ota T, Kobayashi K, Katsura T, Nakamura E (2008) Tourmaline breakdown in a pelitic system:
812 implications for boron cycling through subduction zones. Contrib Mineral Petrol 155:19-32.
813
814 Pabst S, Zack T, Savov IP, Ludwig T, Rost D, Tonarini S, Vicenzi EP (2012) The fate of subducted
815 oceanic slabs in the shallow mantle: insights from boron isotopes and light element composition of

metasomatized blueschists from the Mariana forearc. Lithos 132-133:162-179.

Padrón-Navarta JA, López Sánchez-Vizcaíno V, Hermann J, Connolly JAD, Garrido CJ, Gómez-Pugnaire MT, Marchesi C (2013) Tschermak's substitution in antigorite and consequences for phase relations and water liberation in high-grade serpentinites. Lithos 178:186-196

Palmer, MRP (2017) Boron cycling in subduction zones. Elements 13:237-242.

Peacock SM, Hervig RL (1999) Boron isotopic composition of subduction-zone metamorphic rocks. Chem Geol 160:281–290.

Pleuger J, Roller S, Walter JM, Jansen E, Froitzheim N (2007) Structural evolution of the contact between two Penninic nappes (Zermatt-Saas zone and Combin zone, Western Alps) and implications for the exhumation mechanism and paleogeography. Int J Earth Sci 96:229–252.

Putlitz B, Cosca MA, Schumacher JC (2005) Prograde mica $^{40}Ar/^{39}Ar$ growth ages recorded in HP rocks (Syros, Cyclades, Greece). Chem Geol 214:79–98.

Raimondo T, Payne J, Wade B, Lanari P, Clark C, Hand M (2017) Trace element mapping by LA-ICP-MS: assessing geochemical mobility in garnet. Contrib Mineral Petrol 172:17.

Reddy SM, Wheeler J, Cliff RA (1999) The geometry and timing of orogenic extension: an example from the Western Italian Alps. J Metamorph Geol 17:573-589.

Reinecke T (1991) Very-high-pressure metamorphism and uplift of coesite-bearing metasediments

841 from the Zermatt-Saas zone western Alps. Eur J Mineral 3:7–17.
842
843 Reinecke T (1998) Prograde high- to ultrahigh-pressure metamorphism and exhumation of oceanic
844 sediments at Lago di Cignana, Zermatt-Saas zone, Western Alps. Lithos 42:147–190.
845
846 Romer RL, Meixner A, Hahne K (2014) Lithium and boron isotopic composition of sedimentary
847 rocks – The role of source history and depositional environment: A 250 Ma record from the Cadomian
848 orogeny to the Variscan orogeny. Gondwana Res 26:1093-1110.
849
850 Rosner M, Erzinger J, Franz G, Trumbull RB (2003) Slab-derived boron isotope signatures in arc
851 volcanic rocks from the Central Andes and evidence for boron isotope fractionation during
852 progressive slab dehydration. Geochem Geophys Geosyst 4. https://doi.org/10.1029/2002GC000438.
853
854 Rosner M, Meixner A (2004) Boron isotopic composition and concentration of ten geological
855 reference materials. Geostandard Geoanal Res 28:431-441.
856
857 Rosner M, Wiedenbeck M, Ludwig T (2008) Composition-induced variations in SIMS instrumental
858 mass fractionation during boron isotope ratio measurements of silicate glasses. Geostandards and
859 Geoanalytical Research 32:27-38.
860
861 Rubatto D, Gebauer D, Fanning M (1998) Jurassic formation and Eocene subduction of the Zermatt–
862 Saas–Fee ophiolites: implications for the geodynamic evolution of the Central and Western Alps.
863 Contrib Mineral Petrol 132:269–287.
864
865 Sanchez-Valle C, Reynard B, Daniel I, Lecuyer C, Martinez I, Chervin JC (2005) Boron isotopic

fractionation between minerals and fluids: new insights from in situ high pressure-high temperature vibrational spectroscopic data. Geochim Cosmochim Acta 69:4301–4313.

Scambelluri M, Müntener O, Ottolini L, Pettke TT, Vannucci R (2004) The fate of B, Cl and Li in subducted oceanic mantle and in the antigorite breakdown fluids. Earth Planet Sci Lett 222:217–234.

Scambelluri M, Tonarini S (2012) Boron isotope evidence for shallow fluid transfer across subduction zones by serpentinized mantle. Geology 40:907-910.

Selverstone J, Sharp ZD (2013) Chlorine isotope constraints on fluid-rock intereactions during subduction and exhumation of the Zermatt-Saas ophiolite. Geochem Geophys Geosyst 14. https://doi:10.1002/ggge.20269.

Sievers NE, Menold CA, Grove M, Coble MA (2017) White mica trace element and boron isotope evidence for distinctive infiltration events during exhumation of deeply subducted continental crust. Int Geol Rev 59:621-638.

Taylor HP (1977) Water/rock interactions and the origin of H_2O in granitic batholiths. J Geol Soc London 133:509-558.

Tonarini S, Leeman WP, Leat PT (2011) Subduction erosion of forearc mantle wedge implicated in the genesis of the South Sandwich Island (SSI) arc: Evidence from boron isotope systematics. Earth Planet Sci Lett 301:275–284.

Trumbull RB, Krienitz MS, Grundmann G, Wiedenbeck M (2009) Tourmaline geochemistry and $\delta^{11}B$ variations as a guide to fluid-rock interaction in the Habachtal emerald deposit, Tauern Window, Austria. Contrib Mineral Petrol 157:411-427.

Trumbull RB, Slack JF (2018) Boron isotopes in the continental crust: Granites, pegmatites, felsic volcanic rocks, and related ore deposits. In: Marschall H, Foster G (eds.), Boron Isotopes, Advances in Isotope Geochemistry, Springer International Publishing, chapter 10, pp 249-272.

Van der Klauw SNGC, Reinecke T, Stöckhert B (1997) Exhumation of ultrahigh-pressure metamorphic oceanic crust from Lago di Cignana, Piemontese zone, western Alps: the structural record in metabasites. Lithos 41:79–102.

Vils F, Pelletier L, Kalt A, Müntener O, Ludwig T (2008) The lithium, boron and beryllium content of serpentinized peridotites from ODP Leg 209 (Sites 1272A and 1274A): Implications for lithium and boron budgets of ocenic lithosphere. Geochim Cosmochim Acta 72:5475-5504.

Warren C, Smye AJ, Kelley SP, Sherlock SC (2012) Using white mica $^{40}Ar/^{39}Ar$ data as a tracer for fluid flow and permeability under high-P conditions: Tauern Window, Eastern Alps. J metamorph Geol 30:63-80.

Wunder B, Meixner A, Romer RL, Wirth R, Heinrich W (2005) The geochemical cycle of boron: constraints from boron isotope partitioning experiments between mica and fluid. Lithos 84:205–216.

Yamaoka K, Ishikawa T, Matsubaya O, Ishiyama D, Nagaishi K, Hiroyasu Y, Chiba H, Kawahata H (2012) Boron and oxygen isotope systematics for a complete section of oceanic crustal rocks in the

915 Oman ophiolite. Geochim Cosmochim Acta 84:543–559.

916

Figure captions

Fig. 1 Simplified geological map of the Lago di Cignana area (after Groppo et al. 2009) with sample locations

Fig. 2 Representative thin section images of the (U)HP samples from Lago di Cignana. (a,b): Garnet-phengite quartzite. (c,d) Eclogite. (e) Retrogressed metabasite. Abbreviations: Grt = garnet, phe = phengite, qz = quartz, omp = omphacite, rt = rutile, ep = epidote, pg = paragonite, amp = amphibole

Fig. 3. Major element mineral chemistry of white mica from the Lago di Cignana (U)HP rocks. (a) Mg# vs Si p.f.u. and (b) Na/(Na+K) vs Si p.f.u. White mica is phengite in samples LC-3 and LC-2a and paragonite in sample LC-1b

Fig. 4. Boron geochemistry systematics of white mica from the Lago di Cignana (U)HP rocks. Error bars are ±10 % for [B] and the external precision of each spot for $\delta^{11}B$ (see Tables 2-4)

Fig. 5: White mica boron geochemistry linked to major element chemistry. (a) [B] vs Mg#, (b) [B] vs Al^{IV} p.f.u., (c) $\delta^{11}B$ vs Mg# and (d) $\delta^{11}B$ vs Si p.f.u.

Fig. 6: Ion microprobe spot locations in phengites from the garnet-phengite quartzite. Analysis number (see Table 2) and $\delta^{11}B$ values are given next to the spot

Fig. 7: Rayleigh distillation model to simulate the compositional evolution during prograde devolatilization and associated loss of boron, accompanied by a decrease in $\delta^{11}B$ values. The black curves start at initial values of [B] = 400 µg/g and $\delta^{11}B$ = +2 ‰ (solid line) and -4 ‰ (stippled line),

942 respectively. The red curve starts at [B] = 750 µg/g and $\delta^{11}B$ = +4 ‰. Numbers denote the fraction
943 of boron that remains in the rock after devolatilization. Error bars for $\delta^{11}B$ values represent the
944 external precision (black) and the accuracy (grey)
945
946 **Fig. 8:** Fluid-rock interaction modelling for peak metamorphic overprint in the garnet-phengite
947 quartzite (sample LC-3; beige circles). Two distinct scenarios are modelled: (a) Boron leaching and
948 (b) boron addition. Starting compositions of mica and fluid are given below the figures. Numbers at
949 the curves mark the fluid/rock ratios. Error bars for $\delta^{11}B$ values represent the external precision
950 (black) and the accuracy (grey)
951
952 **Fig. 9:** Fluid-rock interaction modelling for retrograde metamorphic overprint in samples LC-1b
953 (purple squares) and LC-2a (blue diamonds). Two distinct scenarios are modelled: (a) Boron leaching
954 and (b) boron addition. Starting compositions of mica and fluid are given below the figures. Numbers
955 at the curves mark the fluid/rock ratios. Error bars for $\delta^{11}B$ values represent the accuracy (grey)
956

Fig. 1

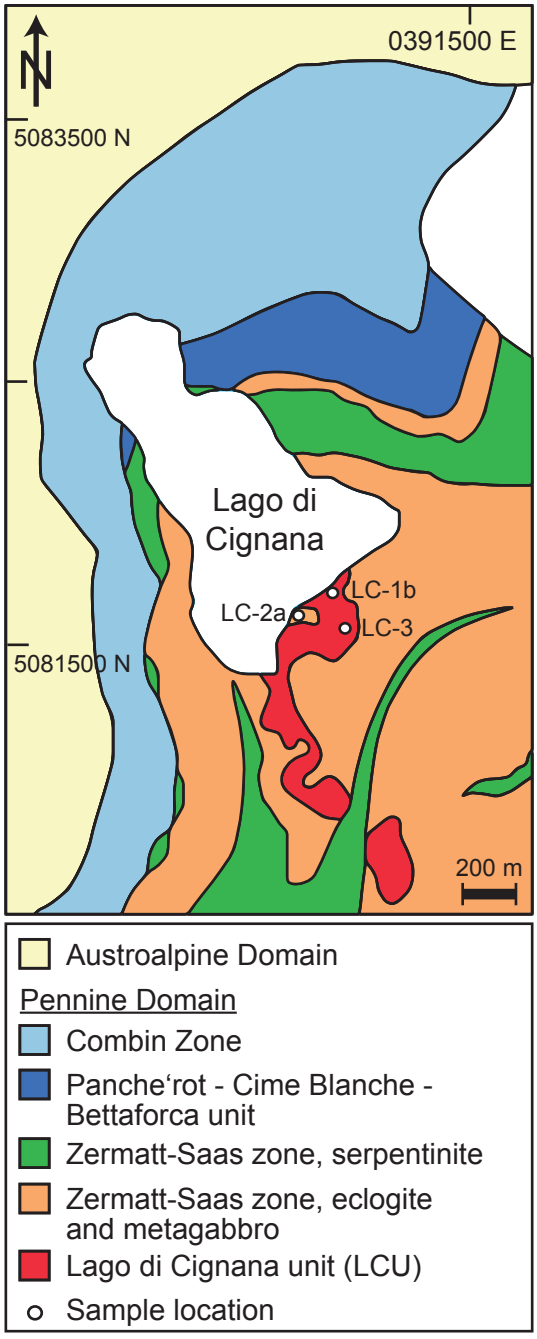
N
0391500 E
5083500 N
5081500 N
Lago di
Cignana
LC-1b
LC-2a
LC-3
200 m
Austroalpine Domain
Pennine Domain
Combin Zone
Panche'rot - Cime Blanche -
Bettaforca unit
Zermatt-Saas zone, serpentinite
Zermatt-Saas zone, eclogite
and metagabbro
Lago di Cignana unit (LCU)
Sample location

Fig.2

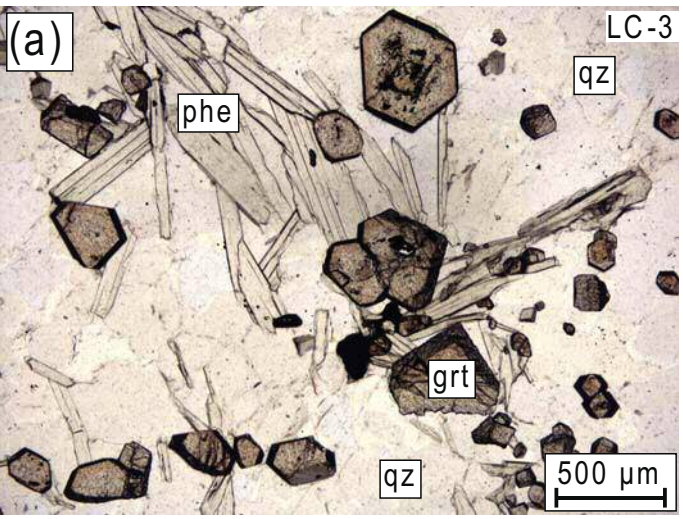
(a)
LC-3
qz
phe
grt
qz
500 μm

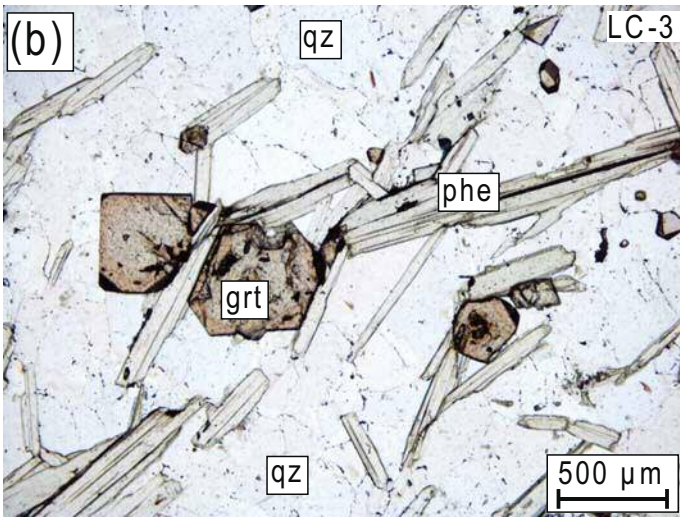
(b)
qz
LC-3
phe
grt
qz
500 μm

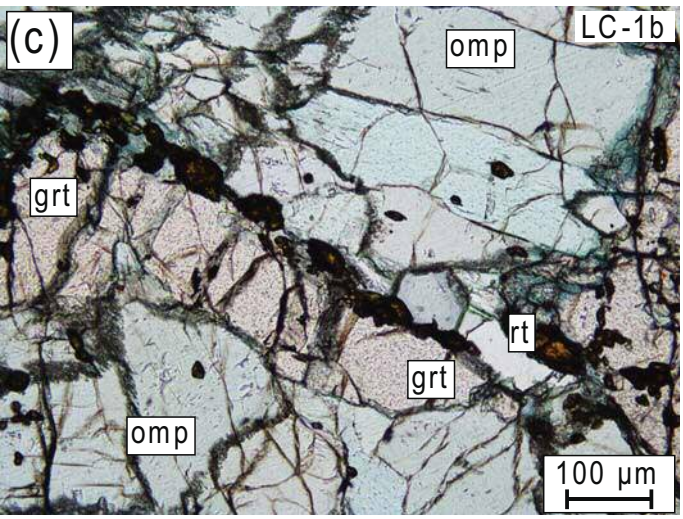
(c)
LC-1b
omp
grt
rt
grt
omp
100 μm

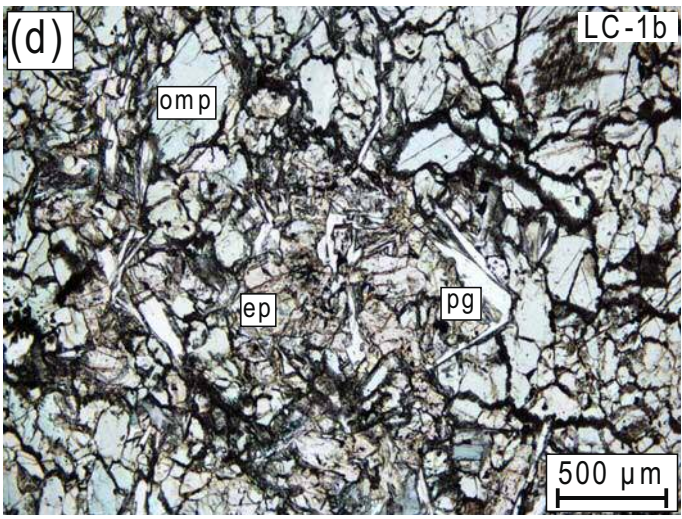
(d)
LC-1b
omp
ep
pg
500 μm

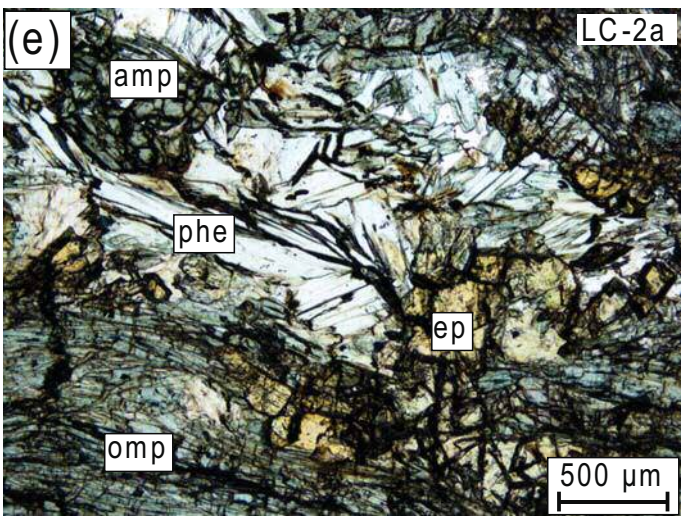
(e)
LC-2a
amp
phe
ep
omp
500 μm

Fig. 3

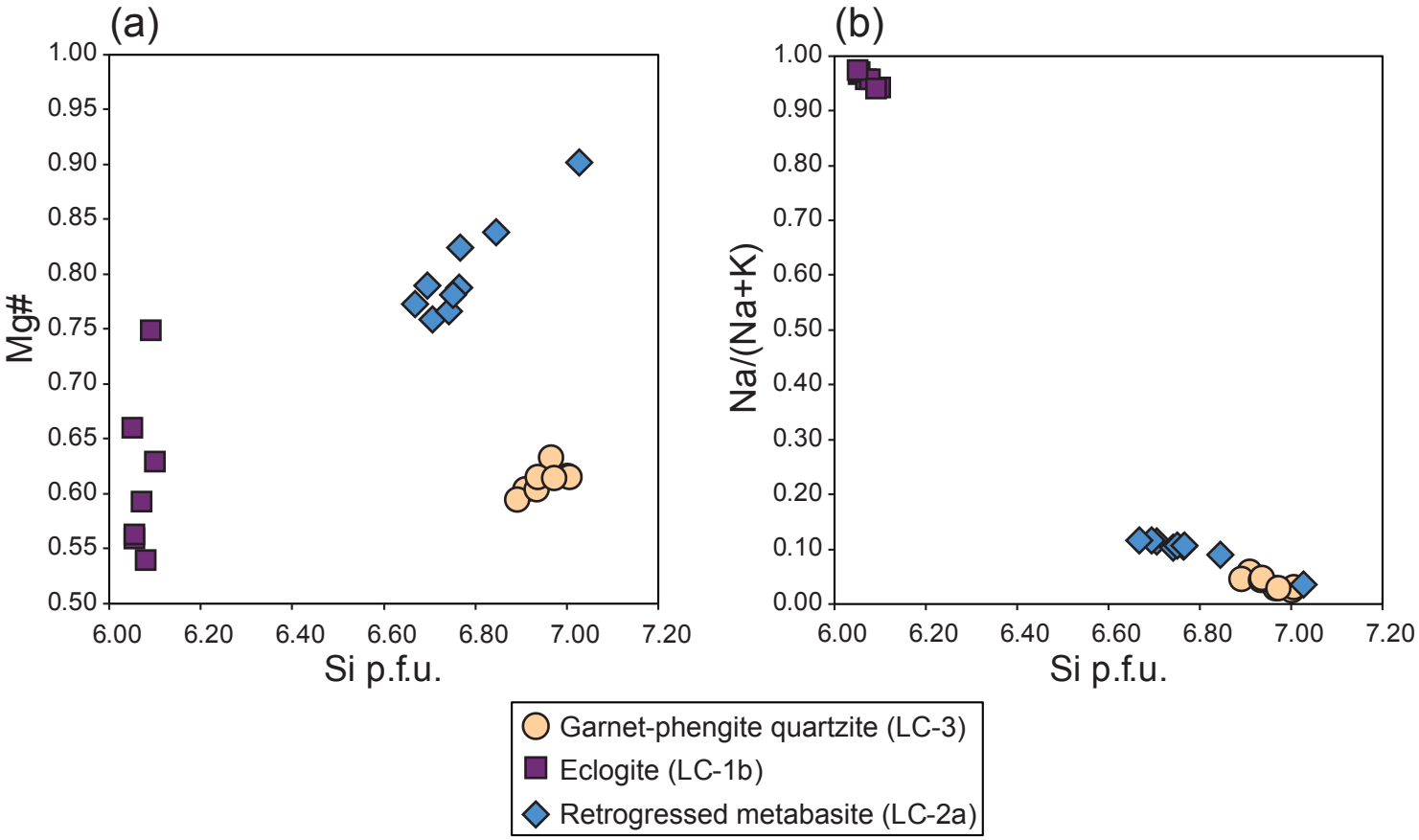
(a)
Mg#
1.00
0.95
0.90
0.85
0.80
0.75
0.70
0.65
0.60
0.55
0.50
6.00
6.20
6.40
6.60
6.80
7.00
7.20
Si p.f.u.
(b)
Na/(Na+K)
1.00
0.90
0.80
0.70
0.60
0.50
0.40
0.30
0.20
0.10
0.00
6.00
6.20
6.40
6.60
6.80
7.00
7.20
Si p.f.u.
Garnet-phengite quartzite (LC-3)
Eclogite (LC-1b)
Retrogressed metabasite (LC-2a)

Fig. 4

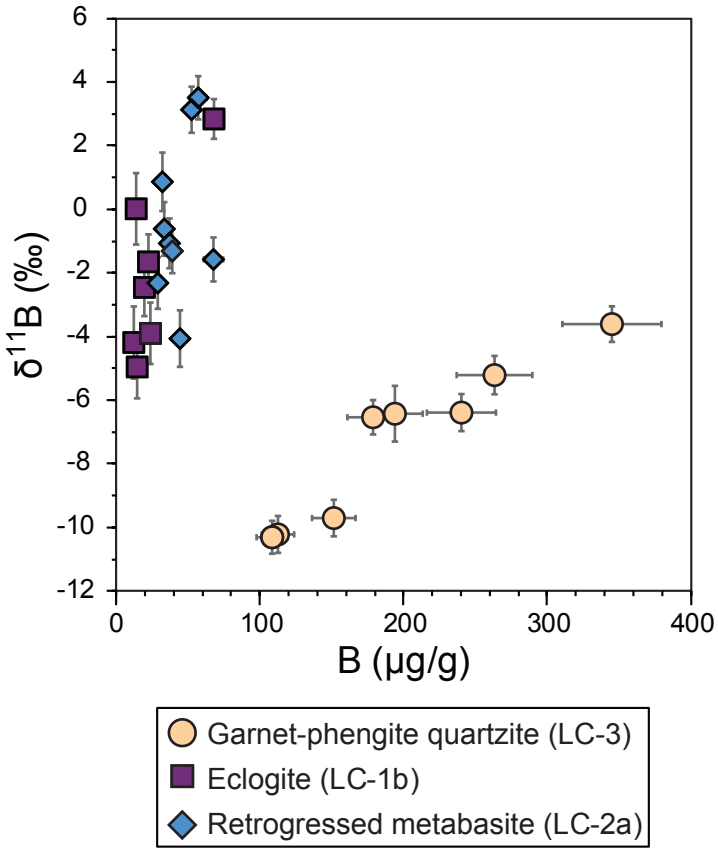
6
4
2
0
-2
-4
-6
-8
-10
-12
0
100
200
300
400
δ11B (‰)
B (µg/g)
Garnet-phengite quartzite (LC-3)
Eclogite (LC-1b)
Retrogressed metabasite (LC-2a)

Fig. 5

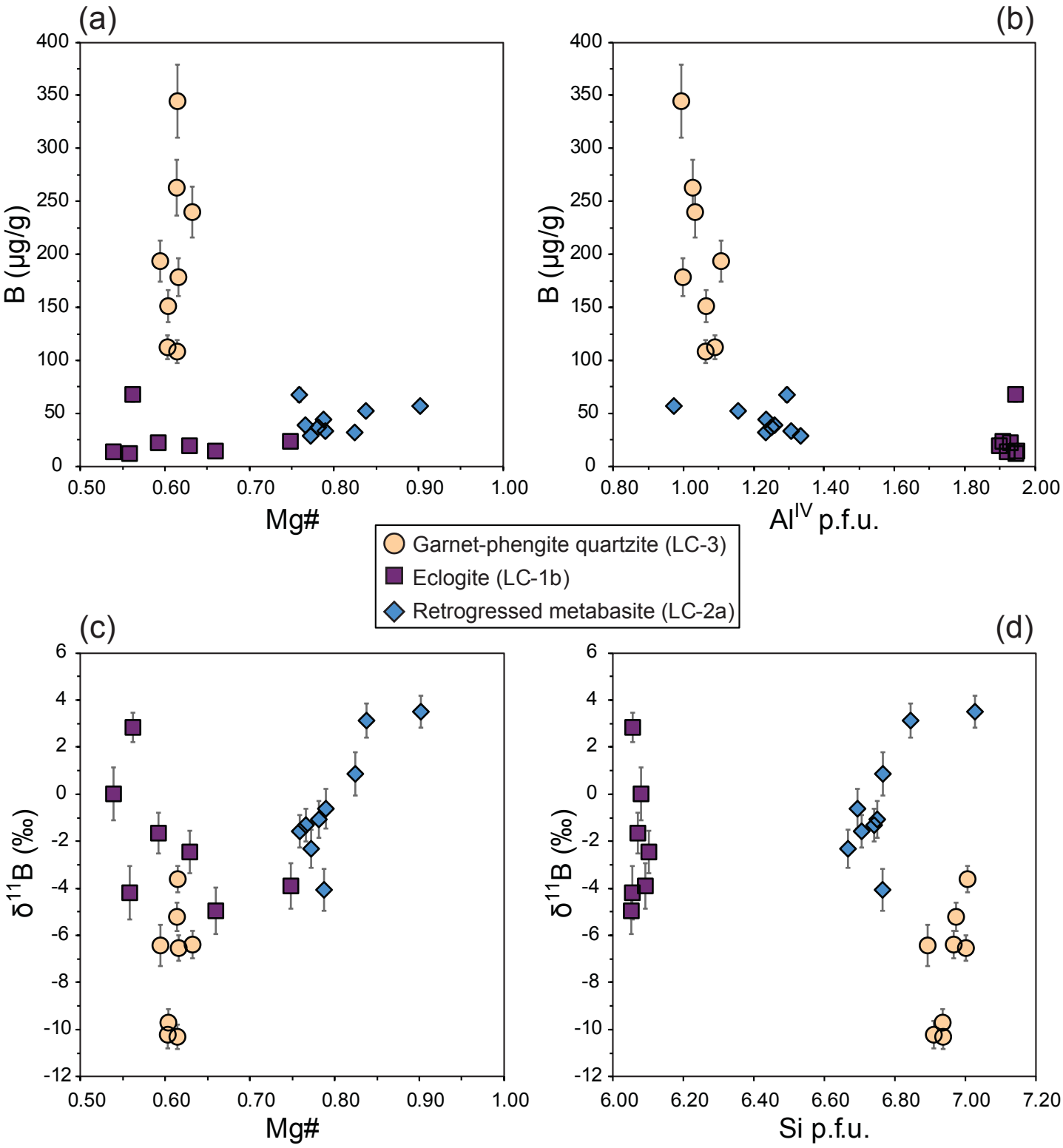
(a)
(b)
(c)
(d)
B (μg/g)
Mg#
Al^IV p.f.u.
δ11B (‰)
Si p.f.u.
Garnet-phengite quartzite (LC-3)
Eclogite (LC-1b)
Retrogressed metabasite (LC-2a)

Fig. 6

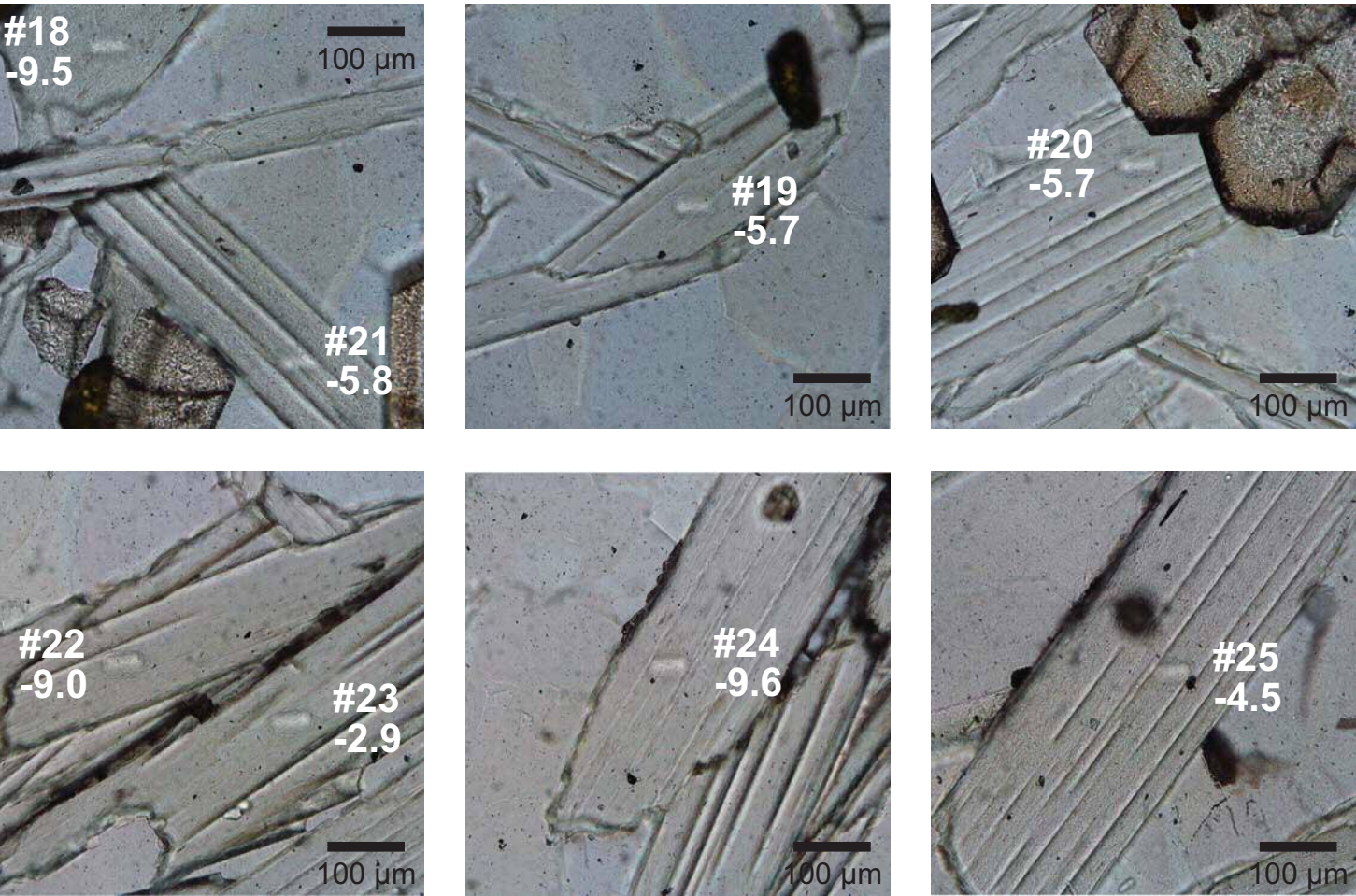
#18
-9.5
100 µm
#21
-5.8
#19
-5.7
100 µm
#20
-5.7
100 µm
#22
-9.0
#23
-2.9
100 µm
#24
-9.6
100 µm
#25
-4.5
100 µm

Fig. 7

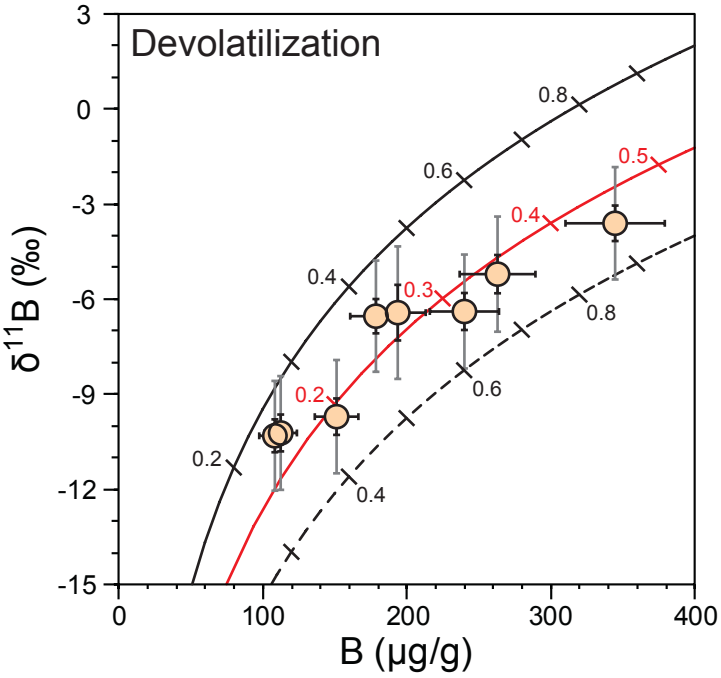
Devolatilization
δ11B (‰)
B (µg/g)
3
0
-3
-6
-9
-12
-15
0
100
200
300
400
0.8
0.6
0.4
0.2
0.5
0.4
0.3
0.2
0.8
0.6
0.4

Fig.8

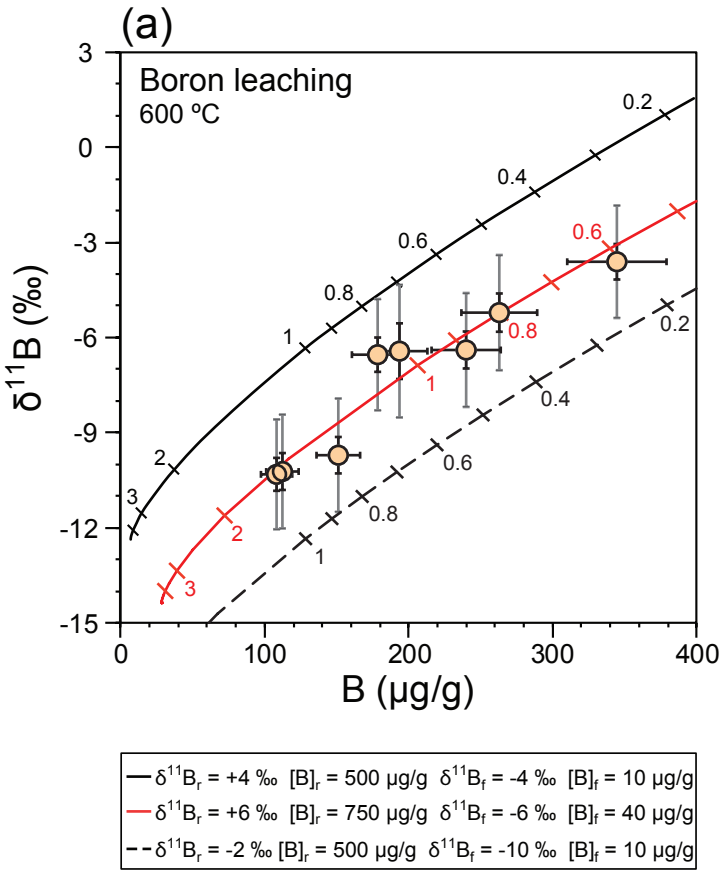
(a)
Boron leaching
600 ºC
δ11B (‰)
B (μg/g)
3
0
-3
-6
-9
-12
-15
0
100
200
300
400
0.2
0.4
0.6
0.8
1
2
3
0.6
0.8
1
0.2
0.4
0.6
0.8
1
2
3
δ11Br = +4 ‰ [B]r = 500 μg/g δ11Bf = -4 ‰ [B]f = 10 μg/g
δ11Br = +6 ‰ [B]r = 750 μg/g δ11Bf = -6 ‰ [B]f = 40 μg/g
δ11Br = -2 ‰ [B]r = 500 μg/g δ11Bf = -10 ‰ [B]f = 10 μg/g

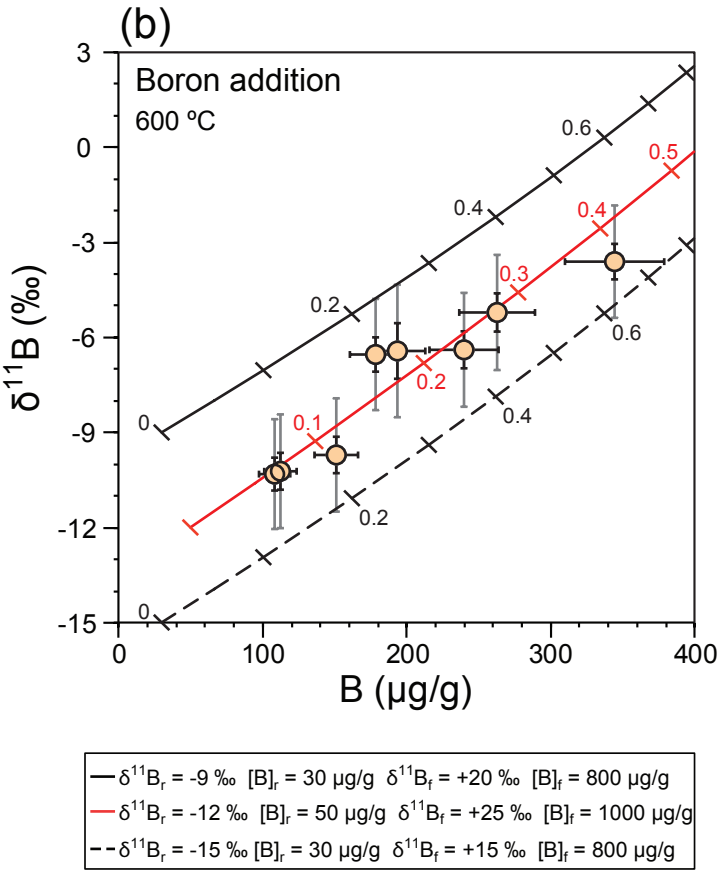
(b)
Boron addition
600 ºC
δ11B (‰)
B (μg/g)
3
0
-3
-6
-9
-12
-15
0
100
200
300
400
0.6
0.4
0.2
0
0.5
0.4
0.3
0.2
0.1
0.6
0.4
0.2
0
δ11Br = -9 ‰ [B]r = 30 μg/g δ11Bf = +20 ‰ [B]f = 800 μg/g
δ11Br = -12 ‰ [B]r = 50 μg/g δ11Bf = +25 ‰ [B]f = 1000 μg/g
δ11Br = -15 ‰ [B]r = 30 μg/g δ11Bf = +15 ‰ [B]f = 800 μg/g

Fig.9

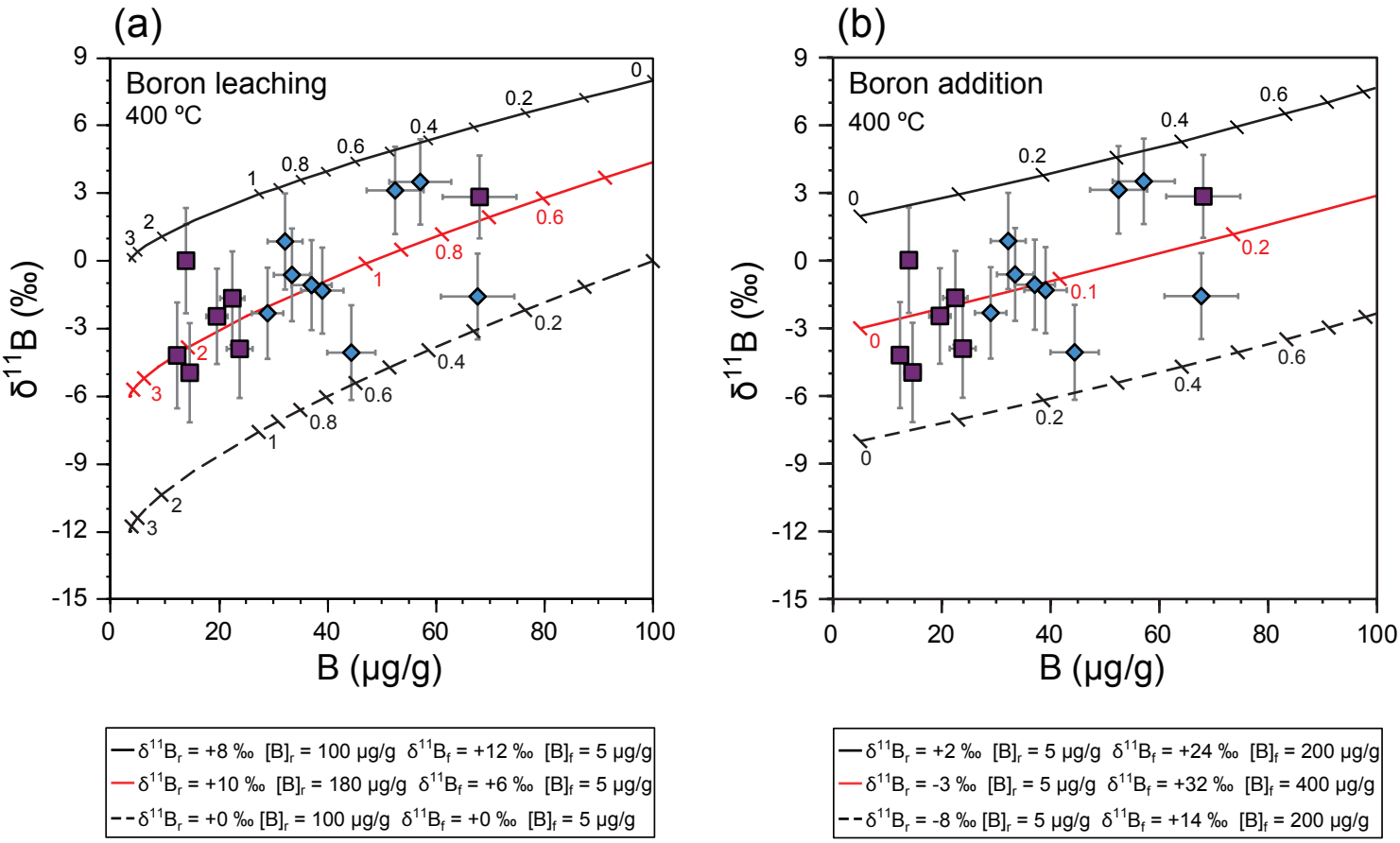
(a)
Boron leaching
400 ºC
δ11B (‰)
B (μg/g)
(b)
Boron addition
400 ºC
δ11B (‰)
B (μg/g)
δ11Br = +8 ‰ [B]r = 100 μg/g δ11Bf = +12 ‰ [B]f = 5 μg/g
δ11Br = +10 ‰ [B]r = 180 μg/g δ11Bf = +6 ‰ [B]f = 5 μg/g
δ11Br = +0 ‰ [B]r = 100 μg/g δ11Bf = +0 ‰ [B]f = 5 μg/g
δ11Br = +2 ‰ [B]r = 5 μg/g δ11Bf = +24 ‰ [B]f = 200 μg/g
δ11Br = -3 ‰ [B]r = 5 μg/g δ11Bf = +32 ‰ [B]f = 400 μg/g
δ11Br = -8 ‰ [B]r = 5 μg/g δ11Bf = +14 ‰ [B]f = 200 μg/g

Table 1 Boron isotope data of measured reference standards

standard	$\delta^{11}B$ (glass)	$\delta^{11}B$ (mica)	1s	n	*$\delta^{11}B$ ± 1s (ref)*	B ppm	1s	*B(ref) ppm*
StHs6/80-G	-4.6 ‰		±0.3 ‰	16	*-4.39 ± 0.13 ‰*[a]	12.5	±0.4	*11.6*[a]
GOR128-G	+13.8 ‰		±0.4 ‰	16	*+13.55 ± 0.11 ‰*[a]	20	±3	*22.7*[a]
GSD1-G	+10.2 ‰		±0.1 ‰	25	*+10.2 ± 0.25 ‰*[b]	67	± 4	*50±20*[b]
mica MVE02-8-5	-6.6 ‰	-5.4 ‰	±0.2 ‰	14	*-2.6 ± 1.7 ‰*[c]	73	±8	*60-140*[c]
phengite 80-3	-14.7 ‰	-13.5 ‰	±0.9 ‰	7	*-13.50 ± 0.35 ‰*[d]	38	±8	*27.1d*[c]
mica JJE01-X-3	-0.7 ‰	+0.5 ‰	±0.3 ‰	8	*-6.3 ± 0.6 ‰c*[d]	291	±48	*30-300*[c]

Data references: [a] Rosner and Meixner (2004); [b] Jochum et al. (2011) ; [c] Martin et al. (2015, 2016); [d] Pabst et al. (2012). 1s uncertainty of $\delta^{11}B$ is standard error of the mean of n repeat measurements.

Table 2 Major element and boron chemistry of white mica from the garnet phengite quartzite (sample LC-3)

SIMS spot number	18	19	20	21	22	23	24	25
wt %								
SiO_2	51.16	51.33	50.72	51.18	51.13	51.18	51.06	51.46
TiO_2	0.22	0.17	0.15	0.15	0.27	0.15	0.12	0.29
Al_2O_3	25.01	24.06	25.12	23.70	24.44	23.75	24.79	24.08
Cr_2O_3	0.03	0.02	0.03	b.d.l.	0.03	b.d.l.	b.d.l.	0.07
FeO	4.01	4.04	4.06	4.11	4.15	4.04	3.89	4.10
MnO	0.07	0.08	0.06	0.04	0.07	0.03	0.07	0.04
MgO	3.42	3.90	3.34	3.70	3.55	3.62	3.48	3.66
CaO	0.02	b.d.l.	b.d.l.	b.d.l.	b.d.l.	0.08	b.d.l.	b.d.l.
Na_2O	0.45	0.22	0.35	0.19	0.33	0.23	0.36	0.21
K_2O	10.98	11.19	11.01	11.22	11.20	11.04	10.90	11.31
Total	95.37	95.01	94.83	94.29	95.17	94.11	94.68	95.22
Cations per formula unit								
Si	6.910	6.967	6.893	7.001	6.935	7.006	6.937	6.974
Al	3.981	3.849	4.023	3.821	3.907	3.832	3.969	3.846
Ti	0.022	0.018	0.015	0.016	0.027	0.015	0.013	0.029
Cr	0.003	0.002	0.003	—	0.003	—	—	0.008
Mg	0.689	0.789	0.677	0.755	0.718	0.739	0.705	0.739
Fe	0.453	0.459	0.461	0.470	0.471	0.463	0.442	0.465
Mn	0.008	0.009	0.007	0.004	0.009	0.003	0.008	0.004
Ca	0.003	—	—	—	—	0.012	—	—
Na	0.118	0.059	0.091	0.051	0.087	0.060	0.095	0.056
K	1.892	1.938	1.909	1.958	1.938	1.928	1.889	1.955
Total	14.080	14.088	14.079	14.077	14.095	14.057	14.058	14.076
Mg#	0.603	0.632	0.595	0.616	0.604	0.615	0.615	0.614
Na/(Na+K)	0.059	0.030	0.046	0.025	0.043	0.030	0.048	0.028
Boron data								
B (µg/g)	113	240	194	179	151	345	109	263
$\delta^{11}B$ (‰)	-10.2	-6.4	-6.4	-6.5	-9.7	-3.6	-10.3	-5.2
External precision ±1s (‰)	0.6	0.6	0.9	0.5	0.6	0.6	0.5	0.6
Accuracy ±1s (‰)	1.8	1.8	2.1	1.8	1.8	1.8	1.7	1.8

b.d.l. = below detection limit

Table 3: Major element and boron chemistry of white mica from the eclogite (sample LC-1b)

SIMS spot number	162	163	164	165	166	167	168
wt %							
SiO_2	47.12	47.60	47.53	47.54	47.40	47.65	47.76
TiO_2	0.06	0.09	0.06	b.d.l.	0.04	0.09	0.06
Al_2O_3	38.67	38.09	38.56	38.96	38.26	39.04	38.13
Cr_2O_3	0.01	0.03	0.03	b.d.l.	b.d.l.	0.04	0.01
FeO	0.23	0.33	0.34	0.22	0.40	0.18	0.32
MnO	0.01	b.d.l.	0.02	b.d.l.	0.03	0.01	b.d.l.
MgO	0.16	0.32	0.27	0.16	0.26	0.20	0.54
CaO	0.21	0.18	0.15	0.19	0.21	0.16	0.17
Na_2O	7.79	7.74	7.91	8.11	7.93	8.12	7.93
K_2O	0.43	0.73	0.55	0.40	0.55	0.34	0.78
Total	94.69	95.10	95.42	95.58	95.08	95.82	95.70
Cations per formula unit							
Si	6.055	6.102	6.071	6.056	6.080	6.052	6.092
Al	5.857	5.755	5.805	5.850	5.784	5.844	5.732
Ti	0.006	0.008	0.006	—	0.004	0.009	0.006
Cr	0.001	0.003	0.003	—	—	0.004	0.001
Mg	0.031	0.061	0.052	0.030	0.050	0.037	0.102
Fe	0.024	0.036	0.036	0.023	0.042	0.019	0.034
Mn	0.001	—	0.003	—	0.003	0.001	—
Ca	0.029	0.024	0.020	0.026	0.029	0.022	0.023
Na	1.941	1.924	1.959	2.003	1.972	2.000	1.961
K	0.071	0.120	0.089	0.065	0.090	0.055	0.127
Total	14.016	14.033	14.043	14.053	14.055	14.042	14.079
Mg#	0.558	0.629	0.592	0.562	0.539	0.660	0.748
Na/(Na+K)	0.965	0.941	0.956	0.969	0.957	0.973	0.939
Boron data							
B (µg/g)	12.3	19.7	22.5	68.1	13.9	14.6	23.8
$\delta^{11}B$ (‰)	-4.2	-2.5	-1.7	2.8	0.0	-5.0	-3.9
External precision ±1s (‰)	1.1	0.9	0.9	0.6	1.1	1.0	1.0
Accuracy ±1s (‰)	2.3	2.1	2.1	1.8	2.3	2.2	2.2

b.d.l. = below detection limit

Table 4: Major element and boron chemistry of white mica from the retrogressed metabasite (sample LC-2a)

SIMS spot number	235	236	237	238	239	240	241	242	243
wt %									
SiO_2	50.58	50.27	50.37	49.78	50.35	51.55	50.63	52.68	50.85
TiO_2	0.13	0.14	0.32	0.15	0.25	0.22	0.08	b.d.l.	0.18
Al_2O_3	27.45	28.25	28.20	28.45	27.60	27.00	27.78	24.33	27.41
Cr_2O_3	0.54	0.53	0.59	0.46	0.57	0.42	0.50	0.92	0.84
FeO	1.63	1.75	1.59	1.65	1.79	1.26	1.68	0.93	1.34
MnO	0.05	0.05	0.01	b.d.l.	b.d.l.	0.02	0.02	0.03	0.03
MgO	3.39	3.09	3.35	3.14	3.29	3.65	3.37	4.80	3.53
CaO	b.d.l.	b.d.l.	b.d.l.	b.d.l.	0.02	b.d.l.	b.d.l.	b.d.l.	b.d.l.
Na_2O	0.82	0.88	0.89	0.92	0.79	0.70	0.83	0.28	0.83
K_2O	10.52	10.41	10.32	10.50	10.33	10.71	10.49	11.34	10.53
Total	95.11	95.37	95.64	95.04	94.99	95.54	95.37	95.31	95.53
Cations per formula unit									
Si	6.765	6.706	6.694	6.667	6.741	6.845	6.750	7.027	6.766
Al	4.327	4.441	4.417	4.491	4.355	4.225	4.365	3.825	4.298
Ti	0.013	0.014	0.032	0.015	0.025	0.022	0.008	—	0.018
Cr	0.057	0.056	0.062	0.049	0.061	0.045	0.052	0.097	0.088
Mg	0.676	0.614	0.664	0.627	0.657	0.722	0.670	0.955	0.700
Fe	0.182	0.195	0.177	0.185	0.200	0.140	0.187	0.104	0.149
Mn	0.006	0.006	0.001	—	—	0.002	0.002	0.003	0.003
Ca	—	—	—	—	0.002	—	—	—	—
Na	0.212	0.228	0.230	0.238	0.205	0.180	0.213	0.072	0.213
K	1.795	1.772	1.750	1.794	1.764	1.814	1.784	1.930	1.787
Total	14.034	14.032	14.025	14.065	14.011	13.996	14.032	14.013	14.023
Mg#	0.788	0.759	0.790	0.772	0.766	0.838	0.781	0.902	0.824
Na/(Na+K)	0.106	0.114	0.116	0.117	0.104	0.090	0.107	0.036	0.107
Boron data									
B (µg/g)	44.4	67.7	33.5	29.0	39.1	52.5	37.1	57.1	32.2
$\delta^{11}B$ (‰)	-4.1	-1.6	-0.6	-2.3	-1.3	3.1	-1.1	3.5	0.9
External precision ±1s (‰)	0.9	0.7	0.8	0.8	0.7	0.7	0.8	0.7	0.9
Accuracy ±1s (‰)	2.1	1.9	2.1	2.0	1.9	1.9	2.0	1.9	2.1

b.d.l. = below detection limit

Supplementary Fig. 1:
Back-scattered electron (BSE) image and element distribution maps for a phengite in the garnet-phengite quartzite (sample LC-3). Boron and major element chemical data are from Table 2.

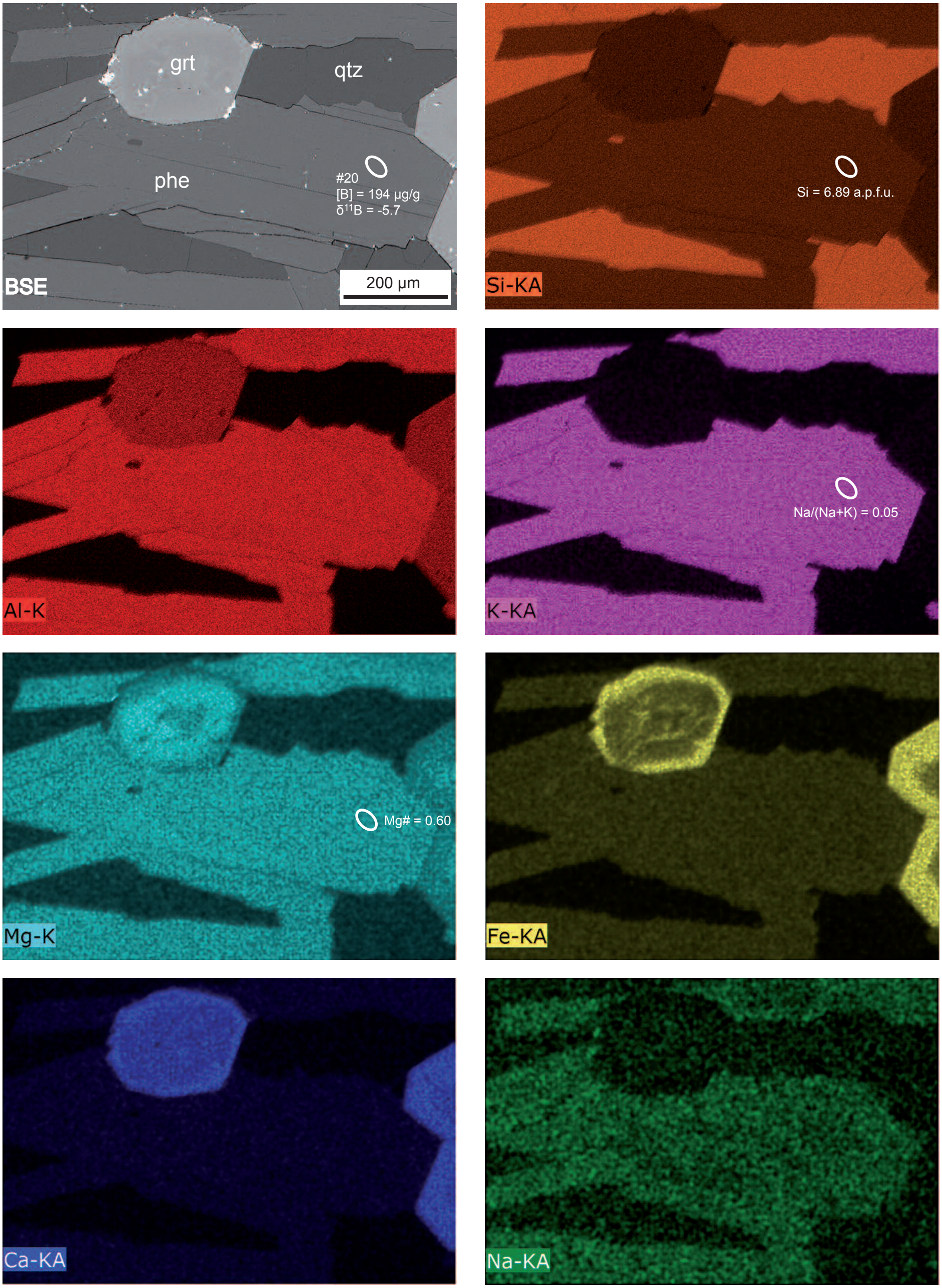

Supplementary Fig. 2:
BSE image and element distribution maps for phengites in the garnet-phengite quartzite (sample LC-3). Boron and major element chemical data are from Table 2.

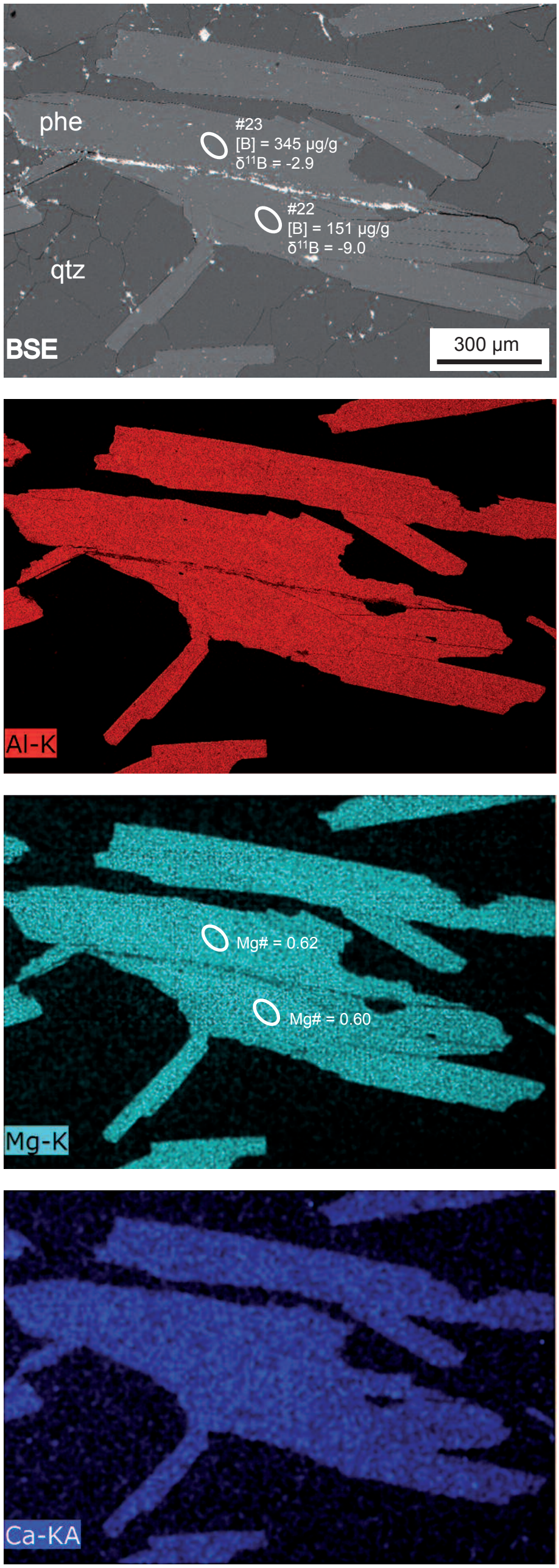

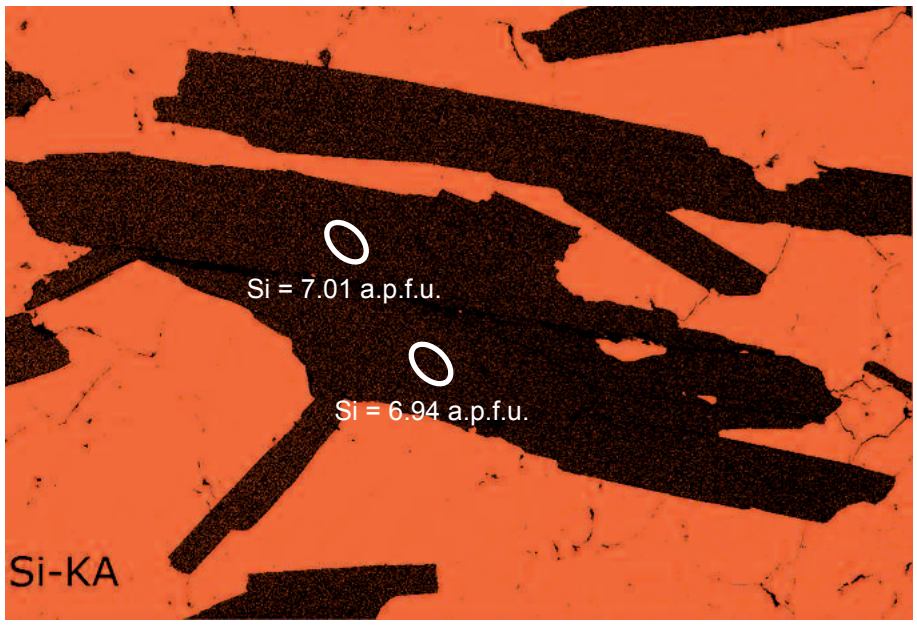

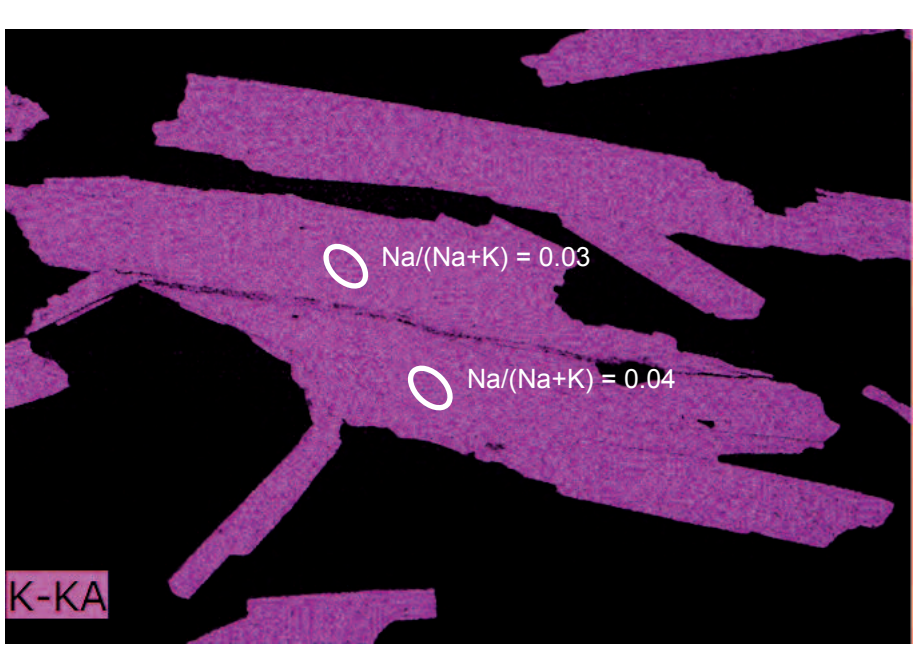

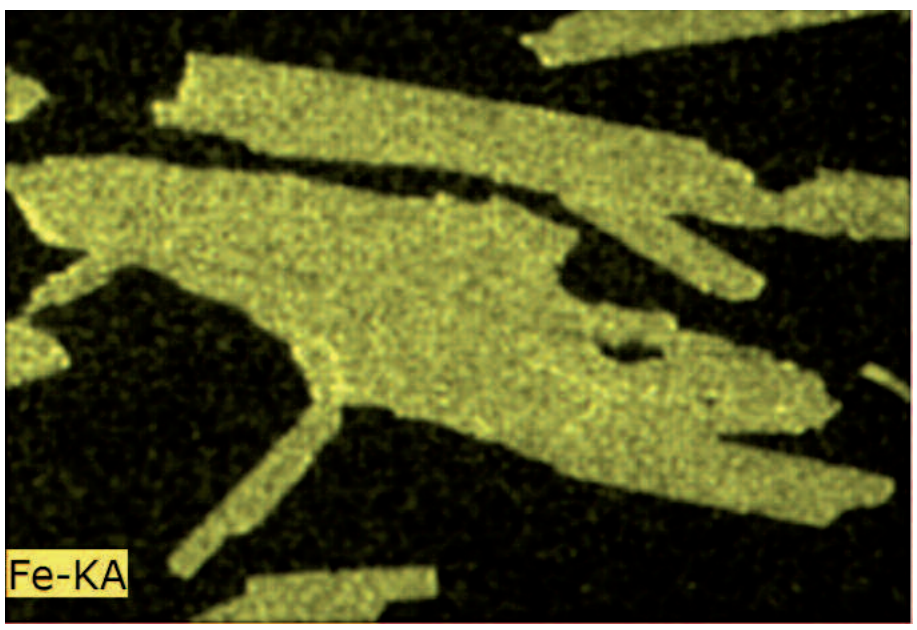

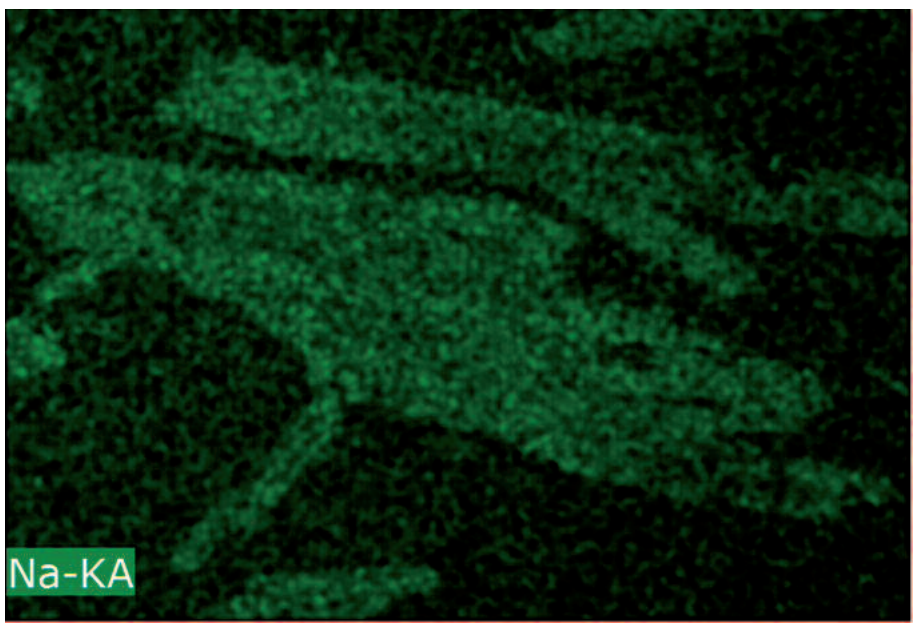

Supplementary Fig. 3:
BSE image and element distribution maps for a paragonite in the eclogite (sample LC-1b). Boron and major element chemical data are from Table 3.

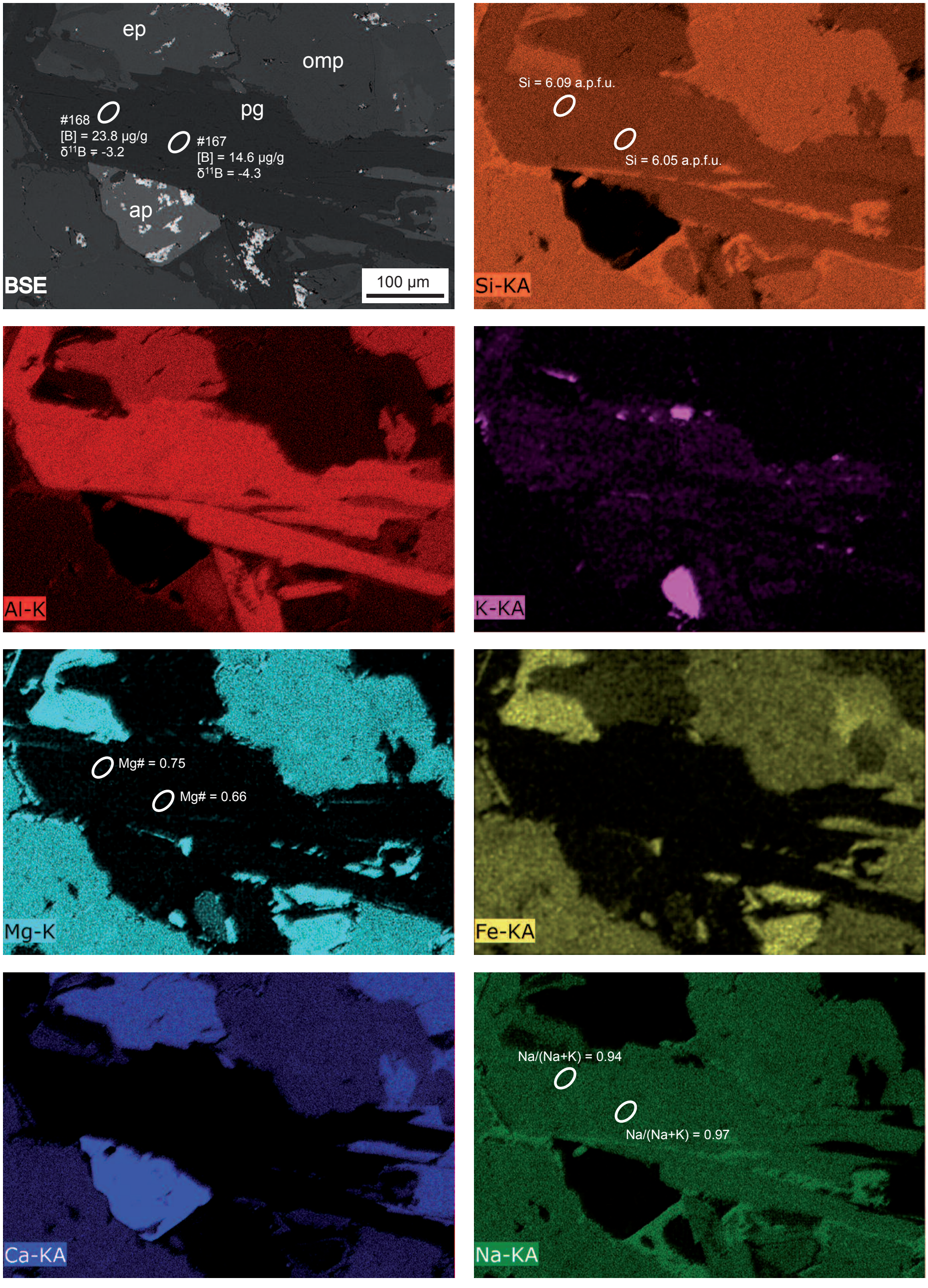

Supplementary Fig. 4:
BSE image and element distribution maps for phengites in the retrogressed metabasite (sample LC-2a). Boron and major element chemical data are from Table 4.